Research Square

Preprints are preliminary reports that have not undergone peer review.
They should not be considered conclusive, used to inform clinical practice,
or referenced by the media as validated information.

Early-Life Stress Drives Anxiety and Irritable Bowel Syndrome-Like Gastrointestinal Dysfunction via Microglial Activation and Gut Microbiota Dysbiosis

min chen
School of Biosciences and Technology, Chengdu Medical College
Yuzhou Xiao
Mental Health Center and National Chengdu Center for Safety Evaluation of Drugs, State Key Laboratory of Biotherapy, West China Hospital of Sichuan University
Can Yang
School of Clinical Medicine & The First Affiliated Hospital of Chengdu Medical College
Xiaodan Pan
Mental Health Center and National Chengdu Center for Safety Evaluation of Drugs, State Key Laboratory of Biotherapy, West China Hospital of Sichuan University
Wenjing Xu
Mental Health Center and National Chengdu Center for Safety Evaluation of Drugs, State Key Laboratory of Biotherapy, West China Hospital of Sichuan University
Yue Zhao
Mental Health Center and National Chengdu Center for Safety Evaluation of Drugs, State Key Laboratory of Biotherapy, West China Hospital of Sichuan University
Xiaofeng Yang
Mental Health Center and National Chengdu Center for Safety Evaluation of Drugs, State Key Laboratory of Biotherapy, West China Hospital of Sichuan University
Dongming Wu
School of Clinical Medicine & The First Affiliated Hospital of Chengdu Medical College
Ying Xu
School of Clinical Medicine & The First Affiliated Hospital of Chengdu Medical College
Liang Wang
liangwang@tmmu.edu.cn

Department of Neurosurgery, Xinqiao Hospital, Army Medical University

Research Article

Keywords: Early-Life Stress, Microglial Activation, Gut Microbiota Dysbiosis, Butyrate, Brain-Gut Axis

Posted Date: June 1st, 2026

DOI: https://doi.org/10.21203/rs.3.rs-9384634/v1

License: This work is licensed under a Creative Commons Attribution 4.0 International License.
Read Full License

Additional Declarations: No competing interests reported.

Abstract

Early-life adversity is a major risk factor for anxiety disorders and functional gastrointestinal diseases, yet how early stress induces persistent dysfunction of the brain-gut axis remains incompletely understood. Here, we show that neonatal maternal separation (MS) induces sustained anxiety-like behaviors in mice and triggers a long-lasting microglia-driven neuroinflammatory state. MS mice exhibited increased microglial activation in the brain, elevated circulating levels of the immunomodulator serotonin (5-HT), and chronic neuroinflammatory responses in both the central nervous system and peripheral circulation. This microglial activation–associated inflammatory state preceded and was closely linked to the progressive development of IBS-like gastrointestinal dysfunction, characterized by visceral hypersensitivity, impaired intestinal barrier integrity, and low-grade intestinal inflammation. These gut abnormalities were accompanied by marked microbial dysbiosis, notably a selective reduction in protective, butyrate-producing taxa such as Faecalibaculum rodentium and Blautia producta, further exacerbating the pro-inflammatory state. Importantly, oral supplementation with sodium butyrate not only restored gut barrier function and microbial balance but also effectively suppressed microglial activation and alleviated anxiety-like behaviors. Collectively, our findings identify microglial activation as a central driver linking early-life stress to chronic inflammation, microbial dysbiosis, and IBS-like gastrointestinal dysfunction. This study highlights microglia–microbiota–butyrate signaling as a critical regulatory axis in brain–gut communication and suggests that targeting microglial-driven inflammation may represent a promising therapeutic strategy for early-life stress–associated anxiety disorders and functional gastrointestinal diseases.

Introduction

Early-life stress, including experiences such as maternal separation and early medical trauma, exerts profound and long-lasting detrimental effects on both mental and physical health across the lifespan (Taylor 2010; Nusslock and Miller 2016; Nakama et al. 2023). Epidemiological and longitudinal studies consistently demonstrate that exposure to stress during sensitive developmental periods markedly increases the risk of neuropsychiatric disorders, including anxiety disorders, depression, post-traumatic stress disorder, and cognitive impairment (McLaughlin et al. 2010; Bale et al. 2010; Modgil et al. 2014; Peña 2026). For instance, exposure to childhood trauma, including neglect or emotional abuse, has been linked to long-term cognitive impairments and a heightened vulnerability to depression in adulthood (Mandelli et al. 2015; Saleh et al. 2017). Beyond psychiatric consequences, individuals with a history of childhood adversity exhibit a substantially elevated risk for a wide spectrum of somatic and functional disorders, particularly those involving dysregulated brain–body interactions (Entringer et al. 2016; Engel et al. 2018; Poplawski et al. 2020; Han et al. 2024).

Precisely how early adversity becomes biologically embedded in the developing brain remains incompletely understood. Experimental studies show that rodents exposed to early-life stress exhibit robust anxiety- and depression-like behaviors, exaggerated persistent alterations in synaptic connectivity within stress- and emotion-related brain regions, such as the prefrontal cortex, hippocampus, and

amygdala (Englund et al. 2021; Hamdan et al. 2022). In addition to alterations in neuronal plasticity, glial cells, the principal immune and homeostatic regulators of the central nervous system (CNS), including microglia and astrocytes, are exquisitely sensitive to environmental stressors during this critical developmental window (Cobb et al. 2016; Delpech et al. 2016; Abbink et al. 2019). Accumulating evidence indicates that neuroimmune dysregulation, particularly aberrant microglial activation, plays a central role in translating early environmental insults into long-term behavioral and physiological abnormalities in adulthood (Beumer et al. 2012; Nusslock and Miller 2016; She et al. 2026).

Microglia, the resident immune cells of the CNS, are highly responsive to early-life stress and can undergo sustained activation, biasing them toward a persistently activated or “primed” phenotype characterized by excessive production of pro-inflammatory cytokines, including IL-1β, TNF-α, and IL-6 (Lesuis et al. 2018; Desplats et al. 2020; Catale et al. 2022; Salinas-García et al. 2024). These cytokines not only disrupt neural circuit maturation and emotional regulation but also influence gastrointestinal function through the bidirectional gut–brain axis, contributing to increased intestinal permeability, serotonergic dysregulation, and visceral hypersensitivity–hallmark features of irritable bowel syndrome (IBS) (Mayer et al. 2014; Hyland et al. 2014; Moloney et al. 2015). Importantly, early-life stress primes microglia into a long-lasting hyper-responsive state, rendering the CNS more susceptible to exaggerated inflammatory responses to subsequent stressors and thereby sustaining chronic dysfunction of the gut–brain axis (Delpech et al. 2015; McKim et al. 2018; Mossad and Erny 2020; Bauer et al. 2022; Zheng et al. 2023).

IBS is a prevalent functional gastrointestinal disorder characterized by recurrent abdominal pain associated with altered bowel habits in the absence of overt structural or biochemical abnormalities (Chey et al. 2015; Sebastián Domingo 2022). Clinically, IBS presents with heterogeneous phenotypes, including diarrhea-predominant (IBS-D), constipation-predominant (IBS-C), mixed (IBS-M), and unclassified subtypes, and is frequently accompanied by bloating, visceral discomfort, anxiety, and depression (Barbara et al. 2011; Spiller and Major 2016; Bisgaard et al. 2023). Therefore, IBS is now recognized as a disorder of gut–brain interaction rather than a purely intestinal disease. At the intestinal level, IBS is associated with increased intestinal permeability, low-grade immune activation, mast cell infiltration and degranulation, and altered serotonin (5-HT) signaling, all of which contribute to abnormal motility and pain perception (Coates et al. 2004; Spiller and Major 2016; Almadi et al. 2025). In parallel, perturbations of the gut microbiota and its metabolites further exacerbate immune and neural signaling, reinforcing chronic symptoms (Franzosa et al. 2019; Han et al. 2024). The high comorbidity of IBS with anxiety and mood disorders underscores the contribution of central neuroimmune and neuroendocrine mechanisms to disease expression, highlighting IBS as a multisystem disorder driven by integrated neural, immune, and microbial dysfunction.

In this study, we aimed to investigate how early-life stress induces long-term brain–gut axis dysfunction. Using neonatal maternal separation as a model of early-life adversity, we showed that MS elicited persistent anxiety-like behaviors in mice, accompanied by sustained microglial activation and chronic neuroinflammation. This prolonged neuroimmune imbalance led to gut barrier disruption and a reduction

in butyrate-producing microbiota. Importantly, oral butyrate supplementation restored brain–gut axis homeostasis. Together, these findings identified microglial activation as a key mediator linking early-life stress to enduring brain–gut dysfunction and highlighted sodium butyrate as a potential therapeutic strategy.

Materials and Methods

Animals

C57BL/6 pregnant mice were purchased from Dossy (Chengdu, China). Animals were housed under controlled environmental conditions, including a constant ambient temperature of 22 ± 2°C, a relative humidity of 40%–70%, and a 12-h light/12-h dark cycle (lights on at 07:00 and off at 19:00), with ad libitum access to food and water. All animal procedures were approved by the Institutional Animal Care and Use Committee of Chengdu Medical College (approval number: CMC-IACUC-2025079) and were conducted in accordance with the guidelines of the Association for Assessment and Accreditation of Laboratory Animal Care and Use Committee of Chengdu Medical College. All efforts were made to minimize animal suffering.

Neonatal maternal separation

Maternal separation was performed as previously described, with minor modifications (Yang et al. 2012; Teng et al. 2016; Kim et al. 2023). Briefly, all pups in the MS group were separated from their dams for 4 h daily (14:00–18:00) from postnatal day 3 (D3) to postnatal day 24 (D24). During each separation period, pups from the same litter were transferred to a separate cage containing cotton and sawdust bedding to maintain body temperature. After the 4 h separation, pups were returned to their original home cages with the dams. Control pups were reared under standard conditions and were not disturbed except for routine cage maintenance, including bedding changes and the provision of food and water. Following completion of the maternal separation procedure, offspring from both control and MS groups were weaned and housed in same-sex groups of four to five mice per cage.

Measurement of the abdominal withdrawal reflex (AWR) score

The AWR test was performed as previously described, with minor modifications (Wu et al. 2022). Briefly, mice were fasted for 12 h before the experiment and anesthetized with isoflurane for balloon catheter insertion. A distension balloon catheter (6-Fr; 2 mm external diameter) was inserted into the descending colon. Each colorectal distension (CRD) was applied for 10 s, followed by a 20-s rest period. Distension pressures of 20, 30, and 40 mmHg were applied sequentially, with each pressure level repeated three times. After completion of the measurements, the balloon was deflated and removed. Visceral sensory responses to CRD were quantified using the AWR scoring system as follows: 0, no behavioral response

to CRD; 1, brief head movement followed by immobility; 2, contraction of abdominal muscles; 3, lifting of the abdomen; and 4, body arching with elevation of the pelvic structures.

Fecal water content

Fecal water content was measured as previously described (Chen et al. 2023). Briefly, the wet weight of fecal pellets produced by each mouse was collected after the animals were placed individually in empty containers for 4 h. Fecal pellets were counted, wrapped in aluminum foil, and weighed immediately to obtain the wet weight. Subsequently, the fecal samples were dried in a forced-air drying oven (UF160plus; Shanghai Xinmo Automation Equipment Co., Ltd.) at 60°C for 48 h to determine the dry weight. Fecal water content was calculated using the following formula: fecal water content (%) = (fecal wet weight − fecal dry weight) / fecal wet weight × 100%.

Endoscopy

The endoscopic condition was assessed as previously described (Becker et al. 2007). Mice were anesthetized with inhaled isoflurane. After achieving a stable surgical plane of anesthesia, mice were examined using a miniature endoscopic imaging system (Richard Wolf GmbH). The endoscope was gently introduced, and the mucosal surface was visualized under continuous illumination to assess endoscopic morphology and pathological changes. Images were acquired and recorded for subsequent analysis. The murine endoscopic score of colitis severity (MEICS) was assessed based on five parameters: colonic wall thickening, alterations in the vascular pattern, presence of visible fibrin, granularity of the mucosal surface, and stool consistency. Each parameter was scored on a scale of 0–3, yielding a cumulative score ranging from 0 (no signs of inflammation) to 15 (most severe endoscopic inflammation).

Measurement of gastrointestinal transit time (GITT)

Mice were individually housed and orally administered 0.25 mL of a 0.5% sodium methylcellulose solution containing 5% activated charcoal. The bottoms of the cages were lined with white paper to facilitate the detection of charcoal-containing fecal pellets. Mice were then allowed free access to food and water until the appearance of the first charcoal-black fecal pellets. GITT was calculated as the time elapsed from oral gavage to the appearance of the first charcoal-black fecal pellets.

Gut microbiome analysis

Each mouse was individually placed in a sterile, empty cage for 2 h between 10:00 a.m. and 1:00 p.m. for fecal sample collection. To minimize environmental and dietary contamination, mice were deprived of food and water during this period. Fresh fecal pellets were collected from mice in different treatment groups using sterile forceps and immediately snap-frozen at − 80°C until DNA extraction.

Total genomic DNA (gDNA) was extracted from fecal samples using the Magnetic Soil and Stool DNA Kit (Tiangen Biotech, Beijing, China) according to the manufacturer's instructions. Following extraction, gDNA concentration and purity were assessed by spectrophotometry prior to sequencing. Full-length 16S rRNA gene sequencing was performed using the PacBio sequencing platform with universal primers 27F (5'-AGAGTTTGATCMTGGCTCAG-3') and 1492R (5'-ACCTTGTTACGACTT-3'). Sequence reads with ≥ 97% similarity were clustered into operational taxonomic units (OTUs) using USEARCH (v10.0). Taxonomic annotation was conducted using a Naive Bayes classifier implemented in QIIME2. Microbiome analyses, including α-diversity, β-diversity, and intergroup differential analysis, were performed using the BMK Cloud platform (Beijing Biomarker Technologies Co., Ltd., China).

Histological examination

After anesthesia, intestinal tissues were dissected from the mice, including segments of the small intestine (10–15 cm proximal to the cecum) and the large intestine (5–7 cm distal to the cecum). The dissected tissues were washed with PBS to remove intestinal contents and then fixed in 4% paraformaldehyde (PFA). Subsequently, the tissues were embedded in paraffin, sectioned vertically into 5 μm-thick sections, and stained with hematoxylin and eosin. A brightfield whole-slide scanner (Leica Biosystems Aperio GT 450, Germany) equipped with a 40×/NA 0.75 objective, controlled by Scanner Administration Manager (SAM) software. Crypt depth and villus height were measured using Fiji software (version 1.54p) and quantified using GraphPad Prism software (version 9.5.1).

Immunofluorescence

For intestinal tissue preparation, mice were euthanized, and both the small and large intestines were dissected. After washing with PBS, the tissues were fixed in 4% PFA overnight, embedded in paraffin, and sectioned vertically into 5 μm-thick sections. The sections were then deparaffinized with xylene and rehydrated through a graded ethanol series, followed by antigen retrieval by boiling in retrieval solution (10 mM citrate buffer, pH 6.0) for 15 minutes. After cooling to room temperature, the sections were washed with PBS and blocked with blocking buffer (5% BSA and 0.2% Triton X-100 in PBS, pH 7.4) for subsequent immunofluorescence staining.

For brain tissue preparation, mice were euthanized and perfused with PBS followed by 4% PFA. The brains were then post-fixed in 4% PFA overnight and cryoprotected in graded sucrose solutions (10–30% sucrose in PBS) until fully equilibrated. Subsequently, the brains were embedded in OCT compound (Cat#3801481, Leica Biosystems) and sectioned coronally into 20 μm-thick sections on a cryostat microtome (Microm HM550; ThermoFisher). The brain sections were permeabilized with 0.2% Triton X-100 in PBS for 30 min and then blocked with blocking buffer (5% BSA and 0.2% Triton X-100 in PBS, pH 7.4) for 1 h at room temperature before immunofluorescence staining.

The blocked intestinal and brain sections were incubated with primary antibodies diluted in blocking buffer overnight at 4°C. After three washes with PBST (0.5% Triton X-100 in PBS), the sections were

incubated with Alexa Fluor–conjugated secondary antibodies at room temperature for 1 h, protected from light. The sections were then counterstained with DAPI and washed three additional times with PBST, followed by mounting with ProLong™ Gold antifade mountant (Cat#P36934, ThermoFisher).

Fluorescence images were acquired at 22 ± 1 ℃ using either a laser-scanning confocal microscope (Leica microsystems CMS GmbH, Germany) equipped with a 63×/1.4 NA oil-immersion objective and an sCMOS camera, controlled by LAS X software; a spinning-disk confocal super-resolution microscope (Olympus SpinSR10, Shinjuku, Tokyo) equipped with a 20×/NA 0.8 (Olympus) objective and an sCMOS camera, controlled by cellSens software (Olympus, Tokyo); or a fluorescence microscope (Olympus VS200, Shinjuku, Tokyo) equipped with a 20×/NA 0.8 objective and an CMOS camera, controlled by cellSens software (Olympus, Tokyo). The primary antibodies and their working dilutions were as follows: rabbit anti-Iba1 (1:500, Cat#019-19741, FUJIFILM Wako), rat anti-MBP (1:500, Cat#MAB386, Millipore), rabbit anti-NeuN (1:500, Cat#ab177487, Abcam), goat anti-GFAP (1:500, Cat#ab53554, Abcam), and rabbit anti-MUC2 (1:200, Cat#27675-1-AP, Proteintech).

Sholl analysis

Sholl analysis was performed to assess microglial morphological complexity using Imaris software (version 9.6, Bitplane), as previously described with minor modifications (Althammer et al. 2020). Briefly, fluorescence images were acquired at 22 ± 1 ℃ using the z-stack function of a laser-scanning confocal microscope (Leica microsystems CMS GmbH, Germany) equipped with a 63×/1.4 NA oil-immersion objective and an sCMOS camera, controlled by LAS X software. Each z-stack consisted of 20–30 optical sections at fixed intervals. Raw images were used for 3D reconstruction of microglia using Imaris software (version 9.6). Microglial cell surfaces were reconstructed using the Surface module, followed by tracing and 3D reconstruction of cellular processes with the Filament module. Sholl analysis was then conducted using the Display Sholl Intersections plugin, in which the number of intersections was quantified at 1-μm radial intervals from the soma to evaluate microglial process complexity. Parameters, including maximum branch length, number of branch points, branch volume, and the number of intersections per radius, were used for subsequent quantitative analysis.

Immunohistochemistry

Distal colon tissues were embedded in paraffin and sectioned into 5 μm-thick sections. After deparaffinization and rehydration, the slides were immersed in antigen retrieval solution (10 mM citrate buffer, pH 6.0) and boiled for 15 min. The slides were then permeabilized with 0.2% Triton X-100 in PBS for 30 min and blocked with blocking buffer (5% BSA and 0.2% Triton X-100 in PBS, pH 7.4) for 1 h at room temperature. Subsequently, the blocked sections were incubated with a mouse anti-tryptase primary antibody (1:1000, Cat#GB12110, Servicebio) overnight at 4°C. After washing with PBST (0.5% Triton X-100 in PBS), the sections were incubated with a Poly-HRP–conjugated goat anti-mouse secondary antibody (1:500, Cat#GB23301, Servicebio) for 1 h at room temperature. The sections were then rinsed in PBS and incubated with freshly prepared diaminobenzidine (DAB; 1:200, Cat#G1214, Servicebio), with color development for 1 min according to the manufacturer's instructions. Lastly, the

sections were counterstained with hematoxylin, dehydrated in ascending ethanol and xylene, and mounted with xylene. Slides were scanned in brightfield mode at 22 ± 1 ℃ using a microscope (Olympus VS200, Shinjuku, Tokyo) equipped with a 20×/NA 0.8 objective and a CMOS camera, controlled by cellSens software (Olympus, Tokyo). Tryptase-positive cells were measured and quantified using Fiji software (version 1.54p) and GraphPad Prism software (version 9.5.1), respectively.

Enzyme-linked immunosorbent assay (ELISA) assay

For serum ELISA assays, blood was collected into centrifuge tubes via retro-orbital bleeding and allowed to clot for 2 h at room temperature, followed by centrifugation at 5,000 rpm for 20 min at 4°C. The serum (supernatant) was collected for subsequent analysis. Levels of pro-inflammatory cytokines, including TNF-α, IL-1β, and COX-2, as well as the immunomodulator serotonin (5-HT), were measured using ELISA kits (Quanzhou Ruixin Biotechnology Co., Ltd.). For intestinal 5-HT detection, intestinal tissues were excised, weighed to obtain comparable tissue amounts, and lysed in RIPA buffer supplemented with protease inhibitor cocktail (Sangon Biotech, Shanghai, China). The samples were homogenized and centrifuged at 13,000 rpm for 15 min at 4°C, and the supernatants were collected for 5-HT measurement using an ELISA kit (Quanzhou Ruixin Biotechnology Co., Ltd.) according to the manufacturer's instructions. All procedures were performed in accordance with the manufacturer's protocols. Total protein concentrations were determined using a BCA protein assay kit (Cat#DFR-0500, SmartBuffers). Cytokine and 5-HT concentrations were calculated based on absorbance values relative to standard curves and normalized to total protein content.

Western blot

For mouse tissue preparation, mice were anesthetized with isoflurane and perfused with PBS. Immediately after dissection, intestinal tissues and various brain regions were snap-frozen in liquid nitrogen. Total protein was extracted using a total protein extraction kit (Cat#BC3710, Solarbio) according to the manufacturer's instructions. Protein concentrations were determined using Bradford reagent (Cat#E211-01, Vazyme). Equal amounts of protein were separated by SDS-PAGE and transferred onto 0.45- or 0.2-μm PVDF membranes (Cat#IPVH00010 or ISEQ00010, Millipore) as previously reported with minor modifications (Mahmood and Yang 2012). The membranes were blocked with 5% BSA in TBS buffer and incubated with primary antibodies overnight at 4°C. After washing, the membranes were incubated with HRP-conjugated secondary antibodies. Immunoreactive bands were visualized at the RT using WesternBright™ ECL chemiluminescent substrate (Cat#WBKLS0500, Millipore). Band intensities were quantified using Fiji software (version 1.54p). The primary antibodies, secondary antibodies, and working dilutions used were listed as follows: rabbit anti-Iba1 (1:200, Cat#019-19741, FUJIFILM Wako), rabbit anti-Occludin (1:1000, Cat#27260-1-AP, Proteintech), mouse anti-E-cadherin (1:1000, Cat#610181, BD Biosciences), rabbit anti-GAPDH (1:10,000, Cat#30202ES40, Yeason), HRP-linked goat-anti-mouse (1:10,000; Cat#SAM01-1, Jackson Immunoresearch), and HRP-linked goat-anti-rabbit (1:20,000; Cat#SAR01-1, Jackson Immunoresearch). Raw Western blot images from this paper are available in Supplementary Fig. 1.

Real-time quantitative PCR (RT-qPCR)

Fresh tissues were immediately subjected to RNA isolation using the AxyPrep™ Multisource RNA Miniprep Kit (Cat#AP-MN-MS-RNA-50, Axygen) according to the manufacturer's instructions. Total RNA was reverse-transcribed using the PrimeScript™ RT Reagent Kit with gDNA Eraser (Cat#RR047A, Takara) following the manufacturer's protocol. Quantitative PCR was performed using a QuantStudio™ 1 Real-Time PCR System (QS-1; ThermoFisher) with PowerUp™ SYBR™ Green Master Mix (Cat#A25742, ThermoFisher). Primer sequences used in this study are listed in Supplementary Table 1. Mouse *Gapdh* was used as the internal reference gene. Relative gene expression levels were calculated using the $2^{-\Delta\Delta CT}$ method.

Behavioral tests

All behavioral tests were conducted between 09:00 and 17:00 during the light phase of the light/dark cycle. The sample size for behavioral tests was determined by performing an a priori power analysis using G*Power software (version 3.1.9.7; Heinrich Heine University Düsseldorf, Germany), as previously reported (Kadam and Bhalerao 2010). Throughout behavioral testing, investigators were blinded to group assignments, and mice were randomly assigned to experimental groups. To minimize artifacts caused by residual odor cues, all equipment was cleaned with 70% ethanol and hypochlorous acid solution after each test.

Open field test (OFT)

The OFT was performed as our previously reported procedure (Wang et al. 2024a). Briefly, each mouse was placed in the center of an open field chamber (48 × 48 × 31 cm; length × width × height) under a camera mounted above the arena. Mice were allowed to freely explore the chamber for 15 min. Locomotor activity and movement trajectories were automatically recorded and analyzed using EthoVision XT 7.0 software (Noldus Information Technology, Leesburg, VA, USA).

Elevated plus maze test (EPM)

The EPM test was performed as previously described, with minor modifications (Wang et al. 2025). Briefly, the apparatus consisted of two opposing closed arms (30 × 15 cm, length × width) and two opposing open arms (30 × 10 cm, length × width). A central square (10 × 10 cm) connected the open and closed arms. All arms were elevated 50 cm above the floor. At the start of the experiment, each mouse was placed in the center square facing a closed arm, and its activity was recorded for 5 min. The number of open-arm entries, total distance traveled, and time spent in the open arms were analyzed. Data acquisition and analysis were performed using ANY-maze software (Stoelting Co., Ltd., Wood Dale, IL, USA).

Sucrose preference test (SPT)

The SPT was performed as previously described, with minor modifications (Liu et al. 2018). Briefly, before the formal test, mice were habituated to the two-bottle choice paradigm by providing simultaneous access to one bottle containing 2% (w/v) sucrose solution (CAS#57-50-1, Kermel) and one bottle containing pure water for 24 h. After this period, the positions of the two bottles were switched to

prevent side bias, and the mice were allowed to adapt for an additional 24 h. During the formal test, mice were provided with one pre-weighed bottle of 2% sucrose solution and one pre-weighed bottle of pure water for 24 h. At the end of the test period, the remaining volumes (weights) of both bottles were measured to determine fluid consumption. Sucrose preference was calculated using the following formula: sucrose preference (%) = sucrose consumption / (sucrose consumption + water consumption) × 100%.

Tail suspension test (TST)

The TST was performed as previously described, with minor modifications (Liu et al. 2007). Briefly, each mouse was suspended by the tail using adhesive tape affixed approximately 1 cm from the tip of the tail. The mouse was suspended in a white plastic box with the head positioned at least 50 cm above the bottom to prevent contact with any surfaces. Mouse behavior was recorded for 6 min using a video camera. Data acquisition and analysis were performed using ANY-maze software (Stoelting Co., Ltd., Wood Dale, IL, USA). Immobility time was defined as the absence of active movements, excluding those required for respiration, lasting at least 2 consecutive seconds.

Forced swimming test (FST)

The FST was performed as previously described, with minor modifications (Slattery and Cryan 2012). Briefly, the apparatus consisted of a transparent cylindrical container (20 cm in diameter × 45 cm in height) filled with fresh water (23 ± 1°C) to a depth of 30 ± 2 cm, preventing the mice from touching the bottom with their tails or hind limbs. A camera positioned above the cylinder was used for video recording. Each mouse was individually placed into the water and allowed to swim for a total of 6 min. The first 2 min served as an acclimation (training) period, and immobility was recorded during the final 4 min. Mouse behavior, including immobility time, was recorded and analyzed using EthoVision XT 7.0 software (Noldus Information Technology, Leesburg, VA, USA). Immobility was defined as the absence of active escape-directed behaviors, with the mouse remaining floating in the water while making only minimal movements necessary to keep its head above the surface. After the test, mice were removed from the water, gently dried with a towel, and returned to their home cages.

Statistical analysis

All investigators were blinded to the experimental groups during data acquisition, image analysis, and statistical analysis. Before statistical testing, normality was assessed using the Shapiro–Wilk test for all datasets. Homogeneity of variance was evaluated using the *F* test for comparisons between two independent groups and the Brown–Forsythe test for comparisons involving more than two groups. Statistical methods were then selected based on the results of both normality and variance homogeneity testing, as previously reported (Michel et al. 2020). In detail, for comparisons between two independent groups, if the data were normally distributed, an unpaired Student's *t*-test was applied when variances were equal, whereas Welch's *t*-test was used when variances were unequal. For non-normally distributed data, the Mann–Whitney *U* test was used when variances were equal, and the Kolmogorov–Smirnov test was applied when variances were unequal. For comparisons among three independent groups, one-way

ANOVA followed by Tukey's post hoc test was used when the data were normally distributed and met the assumption of equal variances. If the data were normally distributed but violated the equal variance assumption, Welch's ANOVA followed by Dunnett's T3 post hoc test was performed. For non-normally distributed data, the Kruskal–Wallis test was applied regardless of variance homogeneity, followed by Dunn's multiple-comparison test when appropriate.

The quantitative data are presented as bar graphs with mean ± standard deviation (SD), box-and-whisker plots, violin plots, or scatter plots, depending on the data distribution and sample size (Weissgerber et al. 2015). Statistical analyses were performed using GraphPad Prism Software (version 9.5.1), and a P value < 0.05 was considered statistically significant. Details of biological replicates, the results of the normality and variance of homogeneity tests, and the statistical test methods selected based on these results are provided in the Supplementary Table 2 and the corresponding figure legends.

Results

Early-life stress induces anxiety-like behavior accompanied by an increased microglial cell number

How early-life stress leads to abnormal neuronal behaviors and gastrointestinal disorders remains largely unknown. To investigate the mechanisms underlying early-life stress–induced brain–gut dysfunction, we employed a well-established rodent model of early-life stress, neonatal maternal separation (MS) in mice. Neonatal mice were separated from their mothers for 4 hours daily from postnatal days 3 to 24, a critical period for neurodevelopment, and subsequently subjected to anxiety-related behavioral tests in adulthood (Fig. 1A). Compared with control mice reared under standard conditions, MS mice exhibited reduced body weight during the developmental period (Fig. 1B). Despite their lower body weight, the total distance traveled by MS mice in the open field test (OFT) was comparable to that of control mice, indicating intact locomotor activity (Fig. 1C). Although no significant differences were observed in time spent in the center or the number of center entries in the OFT, MS mice displayed pronounced anxiety-like behavior in the elevated plus maze (EPM). Specifically, MS mice spent more time and traveled a greater distance in the closed arms, accompanied by reduced time spent, fewer entries, and shorter travel distances in the open arms (Figs. 1D-E). Moreover, MS mice also exhibited reduced sucrose preference in the sucrose preference test (SPT) and increased immobility time in the tail suspension test (TST), indicating anhedonia- and despair-like behaviors (Figs. 1F-G). Although no significant difference was observed in the forced swim test (FST) (Fig. 1H), the overall behavioral profile consistently points to heightened anxiety-related behavior in MS mice. Taken together, these findings demonstrate that early-life stress induced by neonatal maternal separation leads to persistent anxiety-like behavioral abnormalities in adulthood.

Next, to explore the cellular basis underlying MS-induced anxiety-like behavior, we first examined the effects of neonatal maternal separation on major brain cell populations. Using immunofluorescence to quantify astrocytes, mature oligodendrocytes, neurons, and microglia, we found that the numbers of

GFAP-labeled astrocytes and NeuN-labeled mature neurons in MS mice were comparable to those in control mice (Figs. 1I-J). In contrast, cortical myelin intensity in MS mice was modestly reduced relative to controls (Fig. 1K). Notably, in addition to changes in oligodendrocytes, microglial cells exhibited a pronounced increase in number in MS mice compared with control mice (Fig. 1L). Together, these findings indicate that early-life stress–induced anxiety-like behavior is closely associated with increased microglial abundance, suggesting that altered microglial homeostasis, including neuroinflammatory activation and/or microglial proliferation or accumulation, may contribute to MS-related behavioral abnormalities.

Evident microglial activation in MS mice drives neuroinflammatory responses in both the central and peripheral systems

Microglia are increasingly recognized as key regulators of anxiety-related behavior through their activation and consequent modulation of neuroinflammatory signaling and neural circuit function (Caetano et al. 2017; Wang et al. 2018; Chen et al. 2024). To determine whether the increased microglial population observed in the MS brain was accompanied by an activated state in response to early-life stress–induced anxiety, microglial morphology was visualized and quantitatively analyzed. As shown in Figs. 2A-D, microglia in the MS group exhibited a hyper-ramified, prime phenotype, characterized by increased total branch length, cellular volume, branch number, and branch points. In addition, the Iba1-labeled microglial intensity and microglial soma size were evidently increased in the MS group, consistent with a heightened responsiveness to secondary challenges, a feature frequently observed following early-life adversity and chronic psychological stress (Gómez-González and Escobar 2010; King et al. 2025). Furthermore, compared with controls, Iba1 expression was markedly elevated in the MS brain at both the transcriptional and translational levels (Figs. 2E-F and Supplementary Fig. 1). Consistent with this activated microglial phenotype, several pro-inflammatory factors, including *Tnf-*, *iNOS*, *Cox-2*, and *Il-1β*, were markedly up-regulated in the MS group (Figs. 2G, H). Collectively, these findings indicate that neonatal maternal separation induces a state of chronic neuroinflammation in the brain that is closely associated with sustained microglial activation.

To further examine the temporal progression of microglial activation following neonatal maternal separation, microglial phenotypes were visualized and quantified at multiple time points, including immediately after separation (postnatal day 24, D24), four weeks after separation (D56), and six weeks after separation (D72). Compared with control mice at the corresponding time points, microglial abundance was significantly increased at D24, followed by a subsequent enlargement of microglial soma size, indicating a gradual and progressive activation of microglia over time (Figs. 2I-K). This sustained microglial activation is consistent with the development of a chronic neuroinflammatory state that may disrupt neuronal function and ultimately contribute to anxiety-like behavior.

In addition to neuroinflammatory alterations within the CNS, elevated inflammatory markers were also detected in the peripheral circulation. Serum levels of the pro-inflammatory mediators TNF-α, COX-2, and IL-1β were also up-regulated in MS mice compared with controls (Fig. 2L). More importantly, serotonin

(5-HT), a key immunomodulatory mediator capable of amplifying neuroimmune and gut–immune signaling, was markedly elevated in the serum of MS mice (Shine et al. 2022; Hung et al. 2025), suggesting the potentially impaired gastrointestinal function after the maternal separation (Fig. 2M). Collectively, these findings indicate neonatal maternal separation induces long-lasting microglial activation and establishes a chronic inflammatory state that extends beyond the brain to the periphery. This persistent neuroimmune and systemic inflammation likely contributes to the emergence of anxiety-like behaviors and gastrointestinal dysfunction following early-life stress.

MS-induced chronic neuroinflammation is accompanied by IBS-like gut dysfunction

To investigate whether elevated 5-HT correlates with gastrointestinal dysfunction, we examined gut-related phenotypes in MS mice. Fecal samples were collected from postnatal day (P)28 to P34 following maternal separation. Analysis of fecal pellets showed that, although the total number of fecal pellets did not differ between groups (Fig. 3A), MS mice exhibited a higher fecal water content compared with controls (Fig. 3B), indicating the presence of a mild diarrhea-like phenotype. Endoscopic examination revealed no gross mucosal abnormalities, such as mucosal thickening, ulceration, or ischemic lesions, and endoscopic scores were comparable between MS and control mice (Fig. 3C). These findings suggest the presence of subtle colonic alterations without macroscopic mucosal injury. Consistent with this, gastrointestinal transit time (GITT) did not differ between groups, indicating that gastrointestinal motility was not clearly affected (Fig. 3D). In contrast, MS mice exhibited a marked increase in abdominal withdrawal reflex (AWR) scores, indicative of enhanced visceral hypersensitivity (Fig. 3E). Additionally, colon length was also slightly reduced in MS mice compared with control mice (Fig. 3F), supporting the presence of chronic gut dysfunction and low-grade intestinal inflammation. Collectively, these results indicate that MS mice develop gastrointestinal dysfunction characterized predominantly by visceral hypersensitivity, in the absence of overt mucosal damage or motility impairment, features that are characteristic of an IBS-like functional gastrointestinal phenotype.

Next, we assessed whether the observed visceral hypersensitivity was associated with intestinal structural damage. H&E staining of the intestine revealed disrupted architecture of the small intestine (SI) in MS mice, characterized primarily by reduced villus height and decreased crypt depth compared with controls (Figs. 3G, H). In addition to the SI, H&E staining of the large intestine (LI) showed a marked reduction in mucin-containing secretory vesicles within goblet cells in MS mice (Fig. 3I). Consistent with this observation, immunofluorescence staining demonstrated evidently decreased expression of the mucus-associated protein MUC2, indicating impairment of the intestinal mucus barrier (Figs. 3J, K). Furthermore, H&E staining of transverse sections of the LI revealed epithelial disruption, including areas of epithelial thinning and focal epithelial loss, in MS mice (Fig. 3L). In contrast, no obvious changes were observed in other organs, such as the heart, liver, and lungs, based on gross morphology and H&E staining (Supplementary Figs. 2A, B). These findings collectively indicate widespread intestinal mucosal barrier disruption and epithelial structural damage in MS mice.

To further characterize intestinal mucosal barrier disruption, we examined the expression of E-cadherin and Occludin, two key components of epithelial adherens and tight junctions, respectively (Kumar et al. 2021). Protein levels of both E-cadherin and Occludin were markedly reduced in MS mice compared with controls, indicating compromised epithelial barrier integrity (Figs. 3M, N, and Supplementary Fig. 1). Given that mast cell–derived tryptase and enterochromaffin cell–derived 5-HT are well-established mediators implicated in IBS pathophysiology, we next investigated whether alterations in these pathways were associated with the observed mucosal barrier damage. Immunohistochemical analysis revealed an increased number of tryptase-positive mast cells in the large intestines of MS mice relative to controls (Figs. 3O, P). In parallel, intestinal 5-HT levels were markedly elevated in MS mice (Fig. 3Q). Finally, these barrier defects were accompanied by elevated mRNA expression of the pro-inflammatory cytokines *Tnf-α* and *Cox-2* (Fig. 3R), suggesting a close association between mucosal barrier disruption and intestinal inflammation.

Collectively, these findings indicate that maternal separation activates mast cell– and enterochromaffin cell–associated signaling pathways, leading to epithelial barrier breakdown and intestinal inflammation. These pathological alterations may act synergistically to enhance visceral hypersensitivity and contribute to the IBS-like phenotype observed in MS mice.

MS-induced gut dysfunction is associated with dysbiosis, leading to a pro-inflammatory state

Since the balance of the gut microbiome is critical for maintaining intestinal integrity and overall gut health, accumulating evidence indicates that microbiome dysbiosis contributes to visceral hypersensitivity, intestinal barrier disruption, and low-grade inflammation in IBS and stress-related gastrointestinal disorders (Paone and Cani 2020; Vicentini et al. 2021; He et al. 2023). To investigate whether MS-induced intestinal dysfunction is associated with alterations in gut microbiota, we performed 16S rRNA sequencing of fecal samples from MS and control mice. Alpha diversity analysis revealed significant alterations in the microbial community structure of MS mice. Rarefaction curves were higher in MS mice, indicating increased overall species richness (Fig. 4A). Consistently, richness estimators such as the Chao1 and ACE indices were significantly elevated, suggesting an increase in rare or low-abundance taxa (Fig. 4B). In contrast, indices reflecting community evenness and dominance showed the opposite trend (Fig. 4C). Both the Shannon and Simpson indices were reduced in MS mice (Fig. 4D), indicating that although more taxa were present, the microbial community became less evenly distributed and was dominated by a limited number of species. Rank abundance curves further demonstrated reduced evenness (Fig. 4E), consistent with an uneven community structure characterized by the expansion of specific taxa alongside numerous low-abundance species. Collectively, this analysis suggested a pronounced gut microbial dysbiosis.

Next, to further identify whether early-life stress induced by maternal separation affects gut microbial composition, the overall community structure was visualized using principal component analysis (PCA). The PCA score plot based on the first two principal components (PC1 and PC2) revealed a clear

separation between control and MS mice, further indicating altered microbial community structures (Fig. 4F). To identify the taxa most responsible for this separation, linear discriminant analysis (LDA) and effect size (LEfSe) analyses were performed. The results revealed that the primary microbial differences between control and MS mouse intestines were largely driven by a reduction in protective bacteria, particularly short-chain fatty acids (SCFAs)-associated beneficial taxa such as Faecalibaculum rodentium, Blautia producta, Parabacteroides goldsteinii, and members of the Atopobiaceae family (Figs. 4G, H). These bacteria are able to produce butyrate, lactate, and acetate, which are critical for maintaining intestinal barrier integrity and exerting anti-inflammatory effects (Fawad et al. 2022; Liu et al. 2024; Wang et al. 2024b; Zhu et al. 2026). Even worse, in addition to the loss of beneficial bacteria, several inflammation-associated taxa, such as Clostridium, Erysipelatoclostridium, Enterococcus, and Clostridioides difficile, were abnormally enriched in the intestines of MS mice, potentially further exacerbating the inflammatory state (Fig. 4G). Collectively, these findings indicate a shift from a protective commensal community toward a proinflammatory microbiome.

Given the observed reduction in beneficial commensals, we further investigated whether MS promoted the expansion of potentially harmful bacteria. Gram-negative bacteria are of particular interest because they contain lipopolysaccharide (LPS), a potent endotoxin that can trigger systemic inflammation and compromise intestinal barrier function (Maldonado et al. 2016; Liu et al. 2025). Analysis of microbial functional profiles revealed a significant increase in gram-negative bacteria in the MS group, suggesting an elevated inflammatory risk (Fig. 4I). Furthermore, predictive functional profiling indicated a minor increase in pathogenic potential in MS mice, reflecting enrichment of microbial pathways associated with virulence and inflammation (Fig. 4J). This shift toward pathogenicity aligns with the observed dysbiosis and may contribute to the inflammatory gut phenotype observed in MS mice. Collectively, these findings indicate that compromised gut integrity in MS mice is closely associated with a shift toward a less beneficial, pro-inflammatory microbiome state (Fig. 4K).

Inhibition of inflammation rescues brain–gut dysfunction–driven anxiety and IBS phenotypes

Given that the observed gut dysbiosis was characterized by a marked reduction in protective bacteria, which are well recognized for their roles in short-chain fatty acid production, such as butyrate, we hypothesized that a resulting deficiency in butyrate availability triggers the inflammatory brain-gut dysfunction observed in MS mice. Accordingly, we next examined whether restoration of the microbial-derived metabolite butyrate could rescue MS-induced neurobehavioral and gastrointestinal abnormalities. To this end, MS-exposed mice were orally administered 200 mM sodium butyrate for 10 consecutive days, followed by behavioral, neuroinflammatory, and intestinal assessments (Fig. 5A). Notably, no evident toxicity of NaB administration was observed in major organs, such as the heart, liver, and lungs, based on gross morphology and H&E staining (Supplementary Figs. 3A, B). Behavioral analyses revealed that sodium butyrate treatment effectively alleviated MS-induced anxiety- and depression-like behaviors. Specifically, the reduced sucrose preference observed in MS mice was markedly restored following butyrate administration (Fig. 5B). In parallel, the increased immobility time in

both the TST and the FST was markedly decreased, indicating a robust rescue of affective behavioral deficits (Figs. 5C, D). Consistent with the behavioral improvements, sodium butyrate treatment profoundly attenuated microglial activation. Both the elevated transcription and translational levels of Iba1 in MS mice were reduced after butyrate treatment (Figs. 5E-G and Supplementary Fig. 1), accompanied by normalization of microglial morphology, characterized by decreased soma size and rescued processes (Figs. 5H-J). These findings suggest that butyrate suppresses MS-induced neuroinflammatory activation of microglia.

Moreover, analysis of proinflammatory cytokines and immunomodulatory mediators revealed that systemic inflammatory and neuroendocrine alterations in MS mice were effectively rescued by butyrate administration. Elevated serum levels of TNF-α, IL-1β, COX-2, and 5-HT observed in MS mice were significantly reduced following butyrate treatment, indicating attenuation of peripheral inflammation and normalization of serotonergic dysregulation (Figs. 5K, L).

More importantly, within the gastrointestinal system, sodium butyrate markedly ameliorated MS-induced intestinal dysfunction. The increased stool water content was significantly reduced (Fig. 5M). In addition, the modest but consistent shortening of colon length in MS mice was reversed, suggesting alleviation of chronic intestinal stress or low-grade inflammation (Fig. 5N). Histological analysis further demonstrated that the pronounced reduction in mucin-containing secretory vesicles within goblet cells, along with decreased mucin expression in MS mice, was effectively restored by butyrate treatment, indicating recovery of the intestinal mucus barrier (Figs. 5O-Q). In parallel, elevated levels of mast cell-derived tryptase were clearly decreased, reflecting reduced mast cell activation (Figs. 5R, S). Consistently, the increased intestinal 5-HT levels observed in MS mice were normalized following butyrate administration (Fig. 5T).

Collectively, these findings demonstrate that sodium butyrate supplementation effectively rescues MS-induced anxiety-like behaviors, microglial activation, systemic inflammation, and gastrointestinal dysfunction. By restoring microglial homeostasis, suppressing mast cell– and enterochromaffin cell–associated signaling, and repairing intestinal barrier integrity, butyrate acts as a critical mediator of brain-gut axis regulation and alleviates the IBS-like phenotype induced by early-life stress.

Discussion

The cellular and molecular mechanisms by which early-life stress leads to persistent brain–gut axis dysfunction remain poorly understood. In this study, we demonstrate that microglia, but not other major CNS cell types, are the earliest and most sensitive responders to early-life stress. Sustained microglial activation induces a chronic neuroinflammatory state in both the central nervous system and the periphery, accompanied by persistent anxiety-like behaviors. This prolonged neuroimmune imbalance progressively disrupts gut barrier integrity, leading to IBS-like features, including reduced expression of intestinal barrier proteins, thinning of the mucus layer, and low-grade intestinal inflammation. These alterations are further associated with gut microbiota dysbiosis, characterized by a loss of SCFA-

producing protective bacteria and an expansion of harmful taxa. Importantly, pharmacological suppression of microglial activation through oral administration of sodium butyrate effectively attenuates neuroinflammation and concurrently ameliorates both anxiety-like behaviors and intestinal dysfunction. Collectively, these findings identify microglial activation as a central neuroimmune mechanism linking early-life stress to enduring brain–gut axis disturbances and highlight sodium butyrate as a promising therapeutic strategy for stress-associated neuropsychiatric and gastrointestinal comorbidities.

Neonatal maternal separation has emerged as a critical risk factor for long-term neuropsychiatric vulnerability, with substantial implications for human health (Niwa et al. 2011; Nishi 2020; Suman et al. 2025; Zhou et al. 2025). Accumulating evidence from human epidemiological studies indicates that early disruption of caregiver–infant interactions, such as parental separation, neglect, or limited mother–newborn contact, is associated with an increased risk of anxiety, depression, cognitive impairments, and neurodevelopmental disorders later in life (Zhang et al. 2023; Zhao et al. 2023; Ren et al. 2023; Ju et al. 2025). Therefore, early-life stress substantially contributes to the global burden of mental illness. Consistent with these observations, animal models of maternal separation, including the present study, provide causal evidence that early-life separation leads to persistent anxiety- and depressive-like behaviors, maladaptive stress responses, and cognitive inflexibility (Mi et al. 2022; Jarrar et al. 2022; Ojha et al. 2024). In addition to behavioral abnormalities, mice exposed to early-life stress also develop IBS-like gastrointestinal dysfunction, highlighting a close interaction between neuropsychiatric outcomes and peripheral gut pathology (Enqi et al. 2021; Bülbül and Sinen 2022; Mallaret et al. 2022).

Current evidence suggests that the long-term behavioral and physiological alterations induced by neonatal maternal separation arise from complex and multifactorial mechanisms, including dysregulation of stress-responsive neuroendocrine systems, altered neurotransmitter signaling, sustained neuroinflammatory activation, and disruption of gut homeostasis (Banqueri et al. 2019; Wong et al. 2019; Hu et al. 2020; Zoubovsky et al. 2020; Nicolas et al. 2022; Yang et al. 2023; Aqaili et al. 2025). Both previous studies and our own findings demonstrate that maternal separation induces robust microglial activation, leading to a persistent inflammatory response in the brain. In particular, the expression of pro-inflammatory mediators, including TNF-α, COX-2, and IL-1β, was markedly elevated in the brains and serum of MS mice, indicating the presence of a systemic inflammatory state (Bachiller et al. 2020; Chen et al. 2025).

In addition to classical pro-inflammatory cytokines, the immune-modulatory neurotransmitter 5-HT was also evidently increased in the circulation, strongly suggesting exaggerated gut dysfunction following early-life stress (Aspesi et al. 2021; Yang et al. 2024). Consistent with previous reports, elevated intestinal and circulating 5-HT levels in MS mice were accompanied by pronounced gastrointestinal abnormalities, supporting a critical role for serotonergic signaling in stress-induced gut dysfunction. As a key signaling molecule at the interface of the gut, immune system, and nervous system, peripheral 5-HT can stimulate intestinal smooth muscle contraction and epithelial secretion by activating 5-HT receptors

on enteric neurons and epithelial cells, thereby promoting increased fluid secretion, enhanced motility, and visceral hypersensitivity (Zhao et al. 2006; Chang et al. 2022).

Moreover, excessive peripheral 5-HT not only amplifies intestinal inflammation but may also indirectly exacerbate microglial activation and dysregulate central stress-related neural circuits, thus contributing to the emergence of anxiety-like behaviors (Margolis and Gershon 2016; Chen et al. 2021; Koopman et al. 2021; Bosáková et al. 2025). This persistent immune and inflammatory state within the central nervous system is likely to further compromise intestinal barrier integrity and alter gut microbiota composition, creating a self-reinforcing cycle of neuroinflammation and gut dysfunction. Together, these findings support a model in which early-life stress induces sustained neuroimmune activation and 5-HT dysregulation, thereby driving long-lasting bidirectional brain–gut axis dysfunction.

Therefore, targeting brain–gut axis dysfunction should be considered a priority for the treatment of early-life stress–induced pathology. Given that gut dysbiosis following early-life adversity is largely attributed to a reduction in butyrate-producing bacteria, and that depletion of endogenous butyrate has been reported in patients with IBS as well as in stress-based animal models (Martin et al. 2024; Li et al. 2024; Zhai et al. 2025), where it contributes to increased intestinal permeability, exaggerated serotonergic signaling, and chronic low-grade inflammation, we further investigated whether supplementation with butyrate could effectively ameliorate brain–gut axis dysfunction. Butyrate is a key short-chain fatty acid required for maintaining intestinal epithelial integrity, regulating mucosal immune responses, and modulating enteric neuronal activity, making it a strong candidate for restoring gut homeostasis and peripheral immune balance (Liang et al. 2022; Singh et al. 2023; Shi et al. 2025).

In the present study, sodium butyrate, acting both as a histone deacetylase (HDAC) inhibitor and as a bioactive signaling metabolite, was found to restrain pro-inflammatory transcriptional programs in microglia and to restore immune homeostasis (Sanaei and Kavoosi 2022). Accordingly, we treated MS mice with oral sodium butyrate. Our findings demonstrate that sodium butyrate treatment effectively suppresses prolonged microglial activation and neuroinflammatory responses induced by neonatal maternal separation, while concurrently alleviating IBS-like gastrointestinal dysfunction and anxiety-like behaviors. These results are consistent with previous reports showing that sodium butyrate improves behavioral and gastrointestinal outcomes in models of depression, chronic stress, and visceral hypersensitivity through normalization of inflammatory cytokine expression and attenuation of microglial reactivity (Huuskonen et al. 2004; Gundersen and Blendy 2009; Xu et al. 2016; Liu et al. 2022; Wang et al. 2022). Importantly, our study highlights the capacity of sodium butyrate to simultaneously target both central and peripheral components of early-life stress pathology, supporting the concept that microbial metabolites represent effective therapeutic modulators of persistent brain–gut axis dysfunction.

In conclusion, this study demonstrates that neonatal maternal separation induces sustained anxiety-like behaviors accompanied by microglia-driven neuroinflammation, elevated circulating serotonin, and progressive IBS-like gastrointestinal dysfunction associated with gut microbial dysbiosis, including a loss of butyrate-producing bacteria. Importantly, oral sodium butyrate supplementation restored gut

barrier integrity and microbial balance while simultaneously suppressing microglial activation and alleviating anxiety-like behaviors. Together, these findings identify microglial activation as a key mechanistic link between early-life stress, chronic inflammation, and gut dysfunction, and highlight the microglia–microbiota–butyrate axis as a promising therapeutic target for brain–gut disorders.

Declarations

Disclosure

The authors declare that they have no known competing financial interests or personal relationships that could have appeared to influence the work reported in this paper.

Funding

This study was supported by the National Natural Science Foundation of China (No. 32571140, China), the Natural Science Foundation of Chongqing (No. CSTB2025NSCQ-GPX0059), and the Grant for Younger PhDs in Xinqiao Hospital (No. WLQNBS).

Author Contribution

Authors' contributionsL.W., Y.X., and D.W.: Writing - Original Draft, Conceptualization, Supervision, Project administration, Funding acquisition. M.C.: Methodology, Validation, Formal analysis, Investigation, Resources, Visualization. Y.X.: Methodology, Investigation, Validation. C.Y., X.P., and W.X.: Methodology, Investigation.

Acknowledgement

AcknowledgementsWe gratefully acknowledge the support of the public equipment platform of West China Hospital, Sichuan University.

Data Availability

Data Availability StatementThe data that support the findings of this study are available from the corresponding author upon reasonable request. All sequencing data generated and analyzed in this study are available in the NCBI Sequence Read Archive (SRA) under BioProject accession number PRJNA1450644. The accession number provides public access to the complete dataset.

References

1. Abbink MR, van Deijk ALF, Heine VM et al (2019) The involvement of astrocytes in early-life adversity induced programming of the brain. Glia 67:1637–1653. https://doi.org/10.1002/GLIA.23625
2. Almadi MK, Sabr MS, Kofi M et al (2025) Epidemiology and Risk Factors of Irritable Bowel Syndrome in the Saudi Population: A Systematic Review. Cureus 17. https://doi.org/10.7759/CUREUS.79974
3. Althammer F, Ferreira-Neto HC, Rubaharan M et al (2020) Three-dimensional morphometric analysis reveals time-dependent structural changes in microglia and astrocytes in the central amygdala and hypothalamic paraventricular nucleus of heart failure rats. J Neuroinflammation 17:1–19. https://doi.org/10.1186/s12974-020-01892-4
4. Aqaili DO, Bendary MA, Almaghrabi SY, Abdelwahab SI (2025) Pathophysiological Mechanisms of Maternal Separation Stress in Cognitive Dysfunction. Saudi J Health Res Pract 1:1–10. https://doi.org/10.63908/TAR9PJ74
5. Aspesi D, Farinetti A, Marraudino M et al (2021) Maternal separation alters the reward system of activity-based anorexia rats. https://doi.org/10.1016/j.psyneuen.2021.105393. Psychoneuroendocrinology 133:
6. Bachiller S, Paulus A, Vázquez-Reyes S et al (2020) Maternal separation leads to regional hippocampal microglial activation and alters the behavior in the adolescence in a sex-specific manner. Brain Behav Immun Health. https://doi.org/10.1016/j.bbih.2020.100142. 9:
7. Bale TL, Baram TZ, Brown AS et al (2010) Early life programming and neurodevelopmental disorders. Biol Psychiatry 68:314–319. https://doi.org/10.1016/J.BIOPSYCH.2010.05.028
8. Banqueri M, Méndez M, Gómez-Lázaro E et al (2019) Early life stress by repeated maternal separation induces long-term neuroinflammatory response in glial cells of male rats. Stress 22:563–570. https://doi.org/10.1080/10253890.2019.1604666
9. Barbara G, Cremon C, De Giorgio R et al (2011) Mechanisms underlying visceral hypersensitivity in irritable bowel syndrome. Curr Gastroenterol Rep 13:308–315. https://doi.org/10.1007/S11894-011-0195-7
10. Bauer KC, York EM, Cirstea MS et al (2022) Gut microbes shape microglia and cognitive function during malnutrition. Glia 70:820–841. https://doi.org/10.1002/GLIA.24139
11. Becker C, Fantini MC, Neurath MF (2007) High resolution colonoscopy in live mice. Nat Protocols 2007 1(6 1):2900–2904. https://doi.org/10.1038/nprot.2006.446
12. Beumer W, Gibney SM, Drexhage RC et al (2012) The immune theory of psychiatric diseases: a key role for activated microglia and circulating monocytes. J Leukoc Biol 92:959–975. https://doi.org/10.1189/JLB.0212100
13. Bisgaard TH, Allin KH, Elmahdi R, Jess T (2023) The bidirectional risk of inflammatory bowel disease and anxiety or depression: A systematic review and meta-analysis. Gen Hosp Psychiatry 83:109–116. https://doi.org/10.1016/J.GENHOSPPSYCH.2023.05.002
14. Bosáková V, Papatheodorou I, Kafka F et al (2025) Serotonin attenuates tumor necrosis factor-induced intestinal inflammation by interacting with human mucosal tissue. Exp Mol Med 57:364–378. https://doi.org/10.1038/S12276-025-01397-1

15. Bülbül M, Sinen O (2022) Centrally Administered Neuropeptide-S Alleviates Gastrointestinal Dysmotility Induced by Neonatal Maternal Separation. Neurogastroenterol Motil 34:e14269. https://doi.org/10.1111/NMO.14269;WGROUP:STRING:PUBLICATION
16. Caetano L, Pinheiro H, Patrício P et al (2017) Adenosine A2A receptor regulation of microglia morphological remodeling-gender bias in physiology and in a model of chronic anxiety. Mol Psychiatry 22:1035–1043. https://doi.org/10.1038/MP.2016.173
17. Catale C, Carola V, Viscomi MT (2022) Early life stress-induced neuroinflammation and neurological disorders: a novel perspective for research. Neural Regen Res 17:1971–1972. https://doi.org/10.4103/1673-5374.335152
18. Chang WY, Yang YT, She MP et al (2022) 5-HT7 receptor-dependent intestinal neurite outgrowth contributes to visceral hypersensitivity in irritable bowel syndrome. Lab Invest 102:1023–1037. https://doi.org/10.1038/s41374-022-00800-z
19. Chen D, Lou Q, Song XJ et al (2024) Microglia govern the extinction of acute stress-induced anxiety-like behaviors in male mice. Nat Commun 15. https://doi.org/10.1038/S41467-024-44704-6
20. Chen F, Hao K, Shu C et al (2025) TRPV1 Suppresses Microglial Inflammatory Activation to Ameliorate Schizophrenia-Associated Behaviors in Maternal Separation Rats. Schizophr Bull. https://doi.org/10.1093/SCHBUL/SBAF153
21. Chen Q, Zhang H, Sun CY et al (2023) Evaluation of two laboratory model methods for diarrheal irritable bowel syndrome. Mol Med 29. https://doi.org/10.1186/S10020-022-00599-X
22. Chen Z, Luo J, Li J et al (2021) Interleukin-33 Promotes Serotonin Release from Enterochromaffin Cells for Intestinal Homeostasis. Immunity 54:151–163e6. https://doi.org/10.1016/J.IMMUNI.2020.10.014
23. Chey WD, Kurlander J, Eswaran S (2015) Irritable bowel syndrome: a clinical review. JAMA 313:949–958. https://doi.org/10.1001/JAMA.2015.0954
24. Coates MD, Mahoney CR, Linden DR et al (2004) Molecular defects in mucosal serotonin content and decreased serotonin reuptake transporter in ulcerative colitis and irritable bowel syndrome. Gastroenterology 126:1657–1664. https://doi.org/10.1053/j.gastro.2004.03.013
25. Cobb JA, O'Neill K, Milner J et al (2016) Density of GFAP-immunoreactive astrocytes is decreased in left hippocampi in major depressive disorder. Neuroscience 316:209–220. https://doi.org/10.1016/J.NEUROSCIENCE.2015.12.044
26. Delpech JC, Madore C, Nadjar A et al (2015) Microglia in neuronal plasticity: Influence of stress. Neuropharmacology 96:19–28. https://doi.org/10.1016/J.NEUROPHARM.2014.12.034
27. Delpech JC, Wei L, Hao J et al (2016) Early life stress perturbs the maturation of microglia in the developing hippocampus. Brain Behav Immun 57:79–93. https://doi.org/10.1016/J.BBI.2016.06.006
28. Desplats P, Gutierrez AM, Antonelli MC, Frasch MG (2020) Microglial memory of early life stress and inflammation: Susceptibility to neurodegeneration in adulthood. Neurosci Biobehav Rev 117:232–242. https://doi.org/10.1016/J.NEUBIOREV.2019.10.013

29. Engel ML, Winiarski DA, Reidy BL, Brennan PA (2018) Early-Life Somatic Complaints: Longitudinal Associations with Maternal and Child Psychopathology. J Dev Behav Pediatr 39:573–579. https://doi.org/10.1097/DBP.0000000000000590
30. Englund J, Haikonen J, Shteinikov V et al (2021) Downregulation of kainate receptors regulating GABAergic transmission in amygdala after early life stress is associated with anxiety-like behavior in rodents. Transl Psychiatry 11. https://doi.org/10.1038/S41398-021-01654-7
31. Enqi W, Jingzhu S, Lingpeng P, Yaqin L (2021) Comparison of the Gut Microbiota Disturbance in Rat Models of Irritable Bowel Syndrome Induced by Maternal Separation and Multiple Early-Life Adversity. Front Cell Infect Microbiol 10:581974. https://doi.org/10.3389/FCIMB.2020.581974/BIBTEX
32. Entringer S, Buss C, Heim C (2016) [Early-life stress and vulnerability for disease in later life]. Bundesgesundheitsblatt Gesundheitsforschung Gesundheitsschutz 59:1255–1261. https://doi.org/10.1007/S00103-016-2436-2
33. Fawad JA, Luzader DH, Hanson GF et al (2022) Histone Deacetylase Inhibition by Gut Microbe-Generated Short-Chain Fatty Acids Entrains Intestinal Epithelial Circadian Rhythms. Gastroenterology 163:1377–1390e11. https://doi.org/10.1053/j.gastro.2022.07.051
34. Franzosa EA, Sirota-Madi A, Avila-Pacheco J et al (2019) Gut microbiome structure and metabolic activity in inflammatory bowel disease. Nat Microbiol 4:293–305. https://doi.org/10.1038/s41564-018-0306-4
35. Gómez-González B, Escobar A (2010) Prenatal stress alters microglial development and distribution in postnatal rat brain. Acta Neuropathol 119:303–315. https://doi.org/10.1007/S00401-009-0590-4
36. Gundersen BB, Blendy JA (2009) Effects of the histone deacetylase inhibitor sodium butyrate in models of depression and anxiety. Neuropharmacology 57:67–74. https://doi.org/10.1016/J.NEUROPHARM.2009.04.008
37. Hamdan JN, Sierra-Fonseca JA, Flores RJ et al (2022) Early-life adversity increases anxiety-like behavior and modifies synaptic protein expression in a region-specific manner. Front Behav Neurosci 16. https://doi.org/10.3389/FNBEH.2022.1008556
38. Han HS, Hwang S, Choi SY et al (2024) Roseburia intestinalis-derived extracellular vesicles ameliorate colitis by modulating intestinal barrier, microbiome, and inflammatory responses. J Extracell Vesicles 13. https://doi.org/10.1002/jev2.12487
39. He KY, Lei XY, Wu DH et al (2023) Akkermansia muciniphila protects the intestine from irradiation-induced injury by secretion of propionic acid. Gut Microbes 15. https://doi.org/10.1080/19490976.2023.2293312
40. Hu P, Maita I, Phan ML et al (2020) Early-life stress alters affective behaviors in adult mice through persistent activation of CRH-BDNF signaling in the oval bed nucleus of the stria terminalis. Transl Psychiatry 10:396–. https://doi.org/10.1038/S41398-020-01070-3;TECHMETA
41. Hung LY, Alves ND, Del Colle A et al (2025) Intestinal Epithelial Serotonin as a Novel Target for Treating Disorders of Gut-Brain Interaction and Mood. Gastroenterology 168:754–768.

https://doi.org/10.1053/J.GASTRO.2024.11.012

42. Huuskonen J, Suuronen T, Nuutinen T et al (2004) Regulation of microglial inflammatory response by sodium butyrate and short-chain fatty acids. Br J Pharmacol 141:874–880. https://doi.org/10.1038/SJ.BJP.0705682;WEBSITE:WEBSITE:BPSPUBS;ISSUE:ISSUE:DOI
43. Hyland NP, Quigley EMM, Brint E (2014) Microbiota-host interactions in irritable bowel syndrome: Epithelial barrier, immune regulation and brain-gut interactions. World J Gastroenterol 8859–8866. https://doi.org/10.3748/wjg.v20.i27.8859
44. Jarrar Q, Ayoub R, Alhussine K et al (2022) Prolonged Maternal Separation Reduces Anxiety State and Increases Compulsive Burying Activity in the Offspring of BALB/c Mice. J Personalized Med 2022 12:12. https://doi.org/10.3390/JPM12111921
45. Ju X, Li X, Guo Q et al (2025) Mental health problems and influencing factors of parent-child separated children: An umbrella review of meta-analysis. J Affect Disord 379:481–488. https://doi.org/10.1016/J.JAD.2025.03.086
46. Kadam P, Bhalerao S (2010) Sample size calculation. Int J Ayurveda Res 1:55. https://doi.org/10.4103/0974-7788.59946
47. Kim EG, Chang W, Shin SY et al (2023) Maternal separation in mice leads to anxiety-like/aggressive behavior and increases immunoreactivity for glutamic acid decarboxylase and parvalbumin in the adolescence ventral hippocampus. Korean J Physiol Pharmacol 27:113–125. https://doi.org/10.4196/KJPP.2023.27.1.113
48. King DP, Abdalaziz M, Majewska AK et al (2025) Microglia Morphology in the Developing Primate Amygdala and Effects of Early Life Stress. https://doi.org/10.1523/ENEURO.0466-24.2024. eNeuro 12:
49. Koopman N, Katsavelis D, Ten Hove AS et al (2021) The multifaceted role of serotonin in intestinal homeostasis. Int J Mol Sci 22. https://doi.org/10.3390/ijms22179487
50. Kumar A, Priyamvada S, Ge Y et al (2021) A Novel Role of SLC26A3 in the Maintenance of Intestinal Epithelial Barrier Integrity. Gastroenterology 160:1240–1255e3. https://doi.org/10.1053/j.gastro.2020.11.008
51. Lesuis SL, Hoeijmakers L, Korosi A et al (2018) Vulnerability and resilience to Alzheimer's disease: early life conditions modulate neuropathology and determine cognitive reserve. Alzheimers Res Ther 10. https://doi.org/10.1186/S13195-018-0422-7
52. Li YJ, Li J, Dai C (2024) Butyrate promotes visceral hypersensitivity in IBS model via mast cell-derived DRG neuron lincRNA-01028-PKC-TRPV1 pathway. https://doi.org/10.1128/MBIO.01533-24. mBio 15:
53. Liang L, Liu L, Zhou W et al (2022) Gut microbiota-derived butyrate regulates gut mucus barrier repair by activating the macrophage/WNT/ERK signaling pathway. Clin Sci (Lond) 136:291–307. https://doi.org/10.1042/CS20210778
54. Liu J, Lv X, Ye T et al (2024) Microbiota-microglia crosstalk between Blautia producta and neuroinflammation of Parkinson's disease: A bench-to-bedside translational approach. Brain Behav

Immun 117:270–282. https://doi.org/10.1016/j.bbi.2024.01.010

55. Liu L, Ling H, Zhang W et al (2022) Functional Comparison of Clostridium butyricum and Sodium Butyrate Supplementation on Growth, Intestinal Health, and the Anti-inflammatory Response of Broilers. Front Microbiol 13:914212. https://doi.org/10.3389/FMICB.2022.914212/BIBTEX
56. Liu MY, Yin CY, Zhu LJ et al (2018) Sucrose preference test for measurement of stress-induced anhedonia in mice. Nat Protocols 2018 13:7. https://doi.org/10.1038/s41596-018-0011-z
57. Liu X, Stancliffe D, Lee S et al (2007) Genetic Dissection of the Tail Suspension Test: A Mouse Model of Stress Vulnerability and Antidepressant Response. Biol Psychiatry 62:81–91. https://doi.org/10.1016/J.BIOPSYCH.2006.08.017
58. Liu Y, Ma P, Liu D et al (2025) Gram-negative intratumoral bacteria mediate lymph node metastasis through LPS-TLR4/MAPK signaling pathway in cervical cancer. J Infect 91. https://doi.org/10.1016/j.jinf.2025.106532
59. Mahmood T, Yang PC (2012) Western Blot: Technique, Theory, and Trouble Shooting. N Am J Med Sci 4:429. https://doi.org/10.4103/1947-2714.100998
60. Maldonado RF, Sá-Correia I, Valvano MA (2016) Lipopolysaccharide modification in Gram-negative bacteria during chronic infection. FEMS Microbiol Rev 40:480–493. https://doi.org/10.1093/femsre/fuw007
61. Mallaret G, Lashermes A, Meleine M et al (2022) Involvement of toll-like receptor 5 in mouse model of colonic hypersensitivity induced by neonatal maternal separation. World J Gastroenterol 28:3903. https://doi.org/10.3748/WJG.V28.I29.3903
62. Mandelli L, Petrelli C, Serretti A (2015) The role of specific early trauma in adult depression: A meta-analysis of published literature. Childhood trauma and adult depression. Eur Psychiatry 30:665–680. https://doi.org/10.1016/J.EURPSY.2015.04.007
63. Margolis KG, Gershon MD (2016) Enteric Neuronal Regulation of Intestinal Inflammation. Trends Neurosci 39:614–624. https://doi.org/10.1016/J.TINS.2016.06.007
64. Martin FP, Cominetti O, Berger B et al (2024) Metabolome-associated psychological comorbidities improvement in irritable bowel syndrome patients receiving a probiotic. Gut Microbes 16. https://doi.org/10.1080/19490976.2024.2347715
65. Mayer EA, Savidge T, Shulman RJ (2014) Brain-gut microbiome interactions and functional bowel disorders. Gastroenterology 146:1500–1512. https://doi.org/10.1053/J.GASTRO.2014.02.037
66. McKim DB, Weber MD, Niraula A et al (2018) Microglial recruitment of IL-1β-producing monocytes to brain endothelium causes stress-induced anxiety. Mol Psychiatry 23:1421–1431. https://doi.org/10.1038/MP.2017.64
67. McLaughlin KA, Green JG, Gruber MJ et al (2010) Childhood adversities and adult psychopathology in the National Comorbidity Survey Replication (NCS-R) III: associations with functional impairment related to DSM-IV disorders. Psychol Med 40:847–859. https://doi.org/10.1017/S0033291709991115

68. Mi X, Zeng GR, Liu JQ et al (2022) Ganoderma Lucidum Triterpenoids Improve Maternal Separation-Induced Anxiety- and Depression-like Behaviors in Mice by Mitigating Inflammation in the Periphery and Brain. Nutrients 2022 14:14. https://doi.org/10.3390/NU14112268
69. Michel MC, Murphy TJ, Motulsky HJ (2020) New author guidelines for displaying data and reporting data analysis and statistical methods in experimental biology. J Pharmacol Exp Ther 372:136–147. https://doi.org/10.1124/JPET.119.264143
70. Modgil S, Lahiri DK, Sharma VL, Anand A (2014) Role of early life exposure and environment on neurodegeneration: implications on brain disorders. Transl Neurodegener 3. https://doi.org/10.1186/2047-9158-3-9
71. Moloney RD, O'Mahony SM, Dinan TG, Cryan JF (2015) Stress-induced visceral pain: toward animal models of irritable-bowel syndrome and associated comorbidities. Front Psychiatry 6. https://doi.org/10.3389/FPSYT.2015.00015
72. Mossad O, Erny D (2020) The microbiota-microglia axis in central nervous system disorders. Brain Pathol 30:1159–1177. https://doi.org/10.1111/BPA.12908
73. Nakama N, Usui N, Doi M, Shimada S (2023) Early life stress impairs brain and mental development during childhood increasing the risk of developing psychiatric disorders. Prog Neuropsychopharmacol Biol Psychiatry 126. https://doi.org/10.1016/J.PNPBP.2023.110783
74. Nicolas S, McGovern AJ, Hueston CM et al (2022) Prior maternal separation stress alters the dendritic complexity of new hippocampal neurons and neuroinflammation in response to an inflammatory stressor in juvenile female rats. Brain Behav Immun 99:327–338. https://doi.org/10.1016/J.BBI.2021.10.016
75. Nishi M (2020) Effects of Early-Life Stress on the Brain and Behaviors: Implications of Early Maternal Separation in Rodents. Int J Mol Sci 2020 21:21. https://doi.org/10.3390/IJMS21197212
76. Niwa M, Matsumoto Y, Mouri A et al (2011) Vulnerability in early life to changes in the rearing environment plays a crucial role in the aetiopathology of psychiatric disorders. Int J Neuropsychopharmacol 14:459–477. https://doi.org/10.1017/S1461145710001239
77. Nusslock R, Miller GE (2016) Early-Life Adversity and Physical and Emotional Health Across the Lifespan: A Neuroimmune Network Hypothesis. Biol Psychiatry 80:23–32. https://doi.org/10.1016/J.BIOPSYCH.2015.05.017
78. Ojha RK, Dongre S, Singh P, Srivastava RK (2024) Late maternal separation provides resilience to chronic variable stress-induced anxiety- and depressive-like behaviours in male but not female mice. World J Biol Psychiatry 25:393–407. https://doi.org/10.1080/15622975.2024.2390411;WGROUP:STRING:PUBLICATION
79. Paone P, Cani PD (2020) Mucus barrier, mucins and gut microbiota: the expected slimy partners? Gut 69:2232–2243. https://doi.org/10.1136/GUTJNL-2020-322260
80. Peña CJ (2026) Epigenetic regulation of brain development, plasticity, and response to early-life stress. Neuropsychopharmacology 51:5–15. https://doi.org/10.1038/S41386-025-02179-Z

81. Poplawski J, Radmilovic A, Montina TD, Metz GAS (2020) Cardiorenal metabolic biomarkers link early life stress to risk of non-communicable diseases and adverse mental health outcomes. Sci Rep 10. https://doi.org/10.1038/S41598-020-69866-3
82. Ren Z, Luo Y, Zheng X, Liu J (2023) Adverse childhood experiences from family and society contribute to increased risk of depressive symptoms and cognitive impairment: a cross-sectional study. Gen Psychiatr 36:e101039. https://doi.org/10.1136/GPSYCH-2023-101039
83. Saleh A, Potter GG, McQuoid DR et al (2017) Effects of early life stress on depression, cognitive performance and brain morphology. Psychol Med 47:171–181. https://doi.org/10.1017/S0033291716002403
84. Salinas-García AF, Roque A, Zamudio-Flores J et al (2024) Early Life Stress Negatively Impacts Spatial Learning Acquisition and Increases Hippocampal CA1 Microglial Activation After a Mild Traumatic Brain Injury in Adult Male Rats. J Neurotrauma 41:514–528. https://doi.org/10.1089/NEU.2023.0452
85. Sanaei M, Kavoosi F (2022) Effect of Sodium Butyrate on p16INK4a, p14ARF, p15INK4b, Class I HDACs (HDACs 1, 2, 3) Class II HDACs (HDACs 4, 5, 6), Cell Growth Inhibition and Apoptosis Induction in Pancreatic Cancer AsPC-1 and Colon Cancer HCT-116 Cell Lines. Asian Pac J Cancer Prev 23:795. https://doi.org/10.31557/APJCP.2022.23.3.795
86. Sebastián Domingo JJ (2022) Irritable bowel syndrome. Med Clin (Barc) 158:76–81. https://doi.org/10.1016/J.MEDCLI.2021.04.029
87. She K, Yuan N, Huang M et al (2026) Emerging role of microglia in the developing dopaminergic system: Perturbation by early life stress. Neural Regen Res 21:126–140. https://doi.org/10.4103/NRR.NRR-D-24-00742
88. Shi J, Mao W, Song Y et al (2025) Butyrate alleviates food allergy by improving intestinal barrier integrity through suppressing oxidative stress-mediated Notch signaling. https://doi.org/10.1002/IMT2.70024. iMeta 4:
89. Shine JM, O'callaghan C, Walpola IC et al (2022) Understanding the effects of serotonin in the brain through its role in the gastrointestinal tract. Brain 145:2967–2981. https://doi.org/10.1093/BRAIN/AWAC256
90. Singh V, Lee GD, Son HW et al (2023) Butyrate producers, The Sentinel of Gut: Their intestinal significance with and beyond butyrate, and prospective use as microbial therapeutics. Front Microbiol 13. https://doi.org/10.3389/FMICB.2022.1103836
91. Slattery DA, Cryan JF (2012) Using the rat forced swim test to assess antidepressant-like activity in rodents. Nature Protocols 2012 7:6 7:1009–1014. https://doi.org/10.1038/nprot.2012.044
92. Spiller R, Major G (2016) IBS and IBD - separate entities or on a spectrum? Nat Rev Gastroenterol Hepatol 13:613–621. https://doi.org/10.1038/NRGASTRO.2016.141
93. Suman PR, Kincheski GC, Frozza RL et al (2025) Neonatal maternal separation causes depressive-like behavior and potentiates memory impairment induced by amyloid-β oligomers in adult mice. Behavioral and Brain Functions 2025 21:1 21:8-. https://doi.org/10.1186/S12993-025-00266-1

94. Taylor SE (2010) Mechanisms linking early life stress to adult health outcomes. Proc Natl Acad Sci U S A 107:8507–8512. https://doi.org/10.1073/PNAS.1003890107
95. Teng W, Chen H, Guo F et al (2016) Expression and distribution of SP and its NK1 receptor in the brain-gut axis in neonatal maternally separated rat model with visceral hypersensitivity. Genet Mol Res 15. https://doi.org/10.4238/GMR.15038999
96. Vicentini FA, Keenan CM, Wallace LE et al (2021) Intestinal microbiota shapes gut physiology and regulates enteric neurons and glia. Microbiome 9. https://doi.org/10.1186/S40168-021-01165-Z
97. Wang L, Yang Z, Satoshi F et al (2024a) Membrane remodeling by FAM92A1 during brain development regulates neuronal morphology, synaptic function, and cognition. Nat Commun 15. https://doi.org/10.1038/S41467-024-50565-W
98. Wang T, Zhou N, Ding F et al (2024b) Xylanase enhances gut microbiota-derived butyrate to exert immune-protective effects in a histone deacetylase-dependent manner. Microbiome 12. https://doi.org/10.1186/s40168-024-01934-6
99. Wang X, Duan C, Li Y et al (2022) Sodium butyrate reduces overnutrition-induced microglial activation and hypothalamic inflammation. Int Immunopharmacol 111:109083. https://doi.org/10.1016/J.INTIMP.2022.109083
100. Wang X, Wang L, Bu Q et al (2025) LUZP1 Regulates Dendritic Spine Maturation and Synaptic Plasticity in the Hippocampal Dentate Gyrus of Mice. https://doi.org/10.1523/JNEUROSCI.1867-24.2025. J Neurosci e1867242025
101. Wang YL, Han QQ, Gong WQ et al (2018) Microglial activation mediates chronic mild stress-induced depressive- and anxiety-like behavior in adult rats. J Neuroinflammation 15. https://doi.org/10.1186/S12974-018-1054-3
102. Weissgerber TL, Milic NM, Winham SJ, Garovic VD (2015) Beyond bar and line graphs: time for a new data presentation paradigm. PLoS Biol 13. https://doi.org/10.1371/JOURNAL.PBIO.1002128
103. Wong HLX, Qin Hyan, Tsang SW et al (2019) Early life stress disrupts intestinal homeostasis via NGF-TrkA signaling. Nat Commun 10. https://doi.org/10.1038/S41467-019-09744-3
104. Wu H, Zhan K, Rao K et al (2022) Comparison of five diarrhea-predominant irritable bowel syndrome (IBS-D) rat models in the brain-gut-microbiota axis. https://doi.org/10.1016/J.BIOPHA.2022.112811. Biomed Pharmacother 149:
105. Xu J, Chen X, Yu S et al (2016) Effects of Early Intervention with Sodium Butyrate on Gut Microbiota and the Expression of Inflammatory Cytokines in Neonatal Piglets. PLoS ONE 11:e0162461. https://doi.org/10.1371/JOURNAL.PONE.0162461
106. Yang D, Bai R, Li C et al (2024) Early-Life Stress Induced by Neonatal Maternal Separation Leads to Intestinal 5-HT Accumulation and Causes Intestinal Dysfunction. J Inflamm Res 17:8945–8964. https://doi.org/10.2147/JIR.S488290
107. Yang JM, Xian YF, Ip PSP et al (2012) Schisandra chinensis reverses visceral hypersensitivity in a neonatal-maternal separated rat model. Phytomedicine 19:402–408. https://doi.org/10.1016/J.PHYMED.2011.11.013

108. Yang Y, Zhong Z, Wang B et al (2023) Activation of D1R signaling in the medial prefrontal cortex rescues maternal separation-induced behavioral deficits through restoration of excitatory neurotransmission. Behav Brain Res 441:114287. https://doi.org/10.1016/J.BBR.2023.114287
109. Zhai L, Zheng Y, Lo CW et al (2025) Butyrate-producing commensal bacteria mediates the efficacy of herbal medicine JCM-16021 on abdominal pain in diarrhea-predominant irritable bowel syndrome: a randomized clinical trial. https://doi.org/10.1016/J.PHYMED.2025.157040. Phytomedicine 145:
110. Zhang T, Kan L, Jin C, Shi W (2023) Adverse childhood experiences and their impacts on subsequent depression and cognitive impairment in Chinese adults: A nationwide multi-center study. J Affect Disord 323:884–892. https://doi.org/10.1016/J.JAD.2022.12.058
111. Zhao A, Urban JF, Morimoto M et al (2006) Contribution of 5-HT2A receptor in nematode infection-induced murine intestinal smooth muscle hypercontractility. Gastroenterology 131:568–578. https://doi.org/10.1053/J.GASTRO.2006.05.013
112. Zhao X, Zhang A, Liu W et al (2023) Childhood separation from parents with cognitive and psychopathological outcomes in adolescence. Dev Sci 26:e13324. https://doi.org/10.1111/DESC.13324
113. Zheng H, Zhang C, Zhang J, Duan L (2023) Sentinel or accomplice: gut microbiota and microglia crosstalk in disorders of gut-brain interaction. Protein Cell 14:726–742. https://doi.org/10.1093/PROCEL/PWAD020
114. Zhou Q, Liang S, Sun Y et al (2025) In-hospital neonatal maternal separation as early-life stress and neurodevelopmental disorders: a cross-sectional and population-based study. Front Psychiatry 16:1572600. https://doi.org/10.3389/FPSYT.2025.1572600/BIBTEX
115. Zhu H, Guo H, Sun N et al (2026) Faecalibaculum rodentium Alleviates Ionizing Radiation-Induced Damage in Mice by Improving Intestinal Integrity and Hematopoiesis via Its Metabolite Butyrate. Adv Sci (Weinh) 13. https://doi.org/10.1002/advs.202509383
116. Zoubovsky SP, Hoseus S, Tumukuntala S et al (2020) Chronic psychosocial stress during pregnancy affects maternal behavior and neuroendocrine function and modulates hypothalamic CRH and nuclear steroid receptor expression. Transl Psychiatry 10:6–. https://doi.org/10.1038/S41398-020-0704-2;TECHMETA

Figures

Figure 1

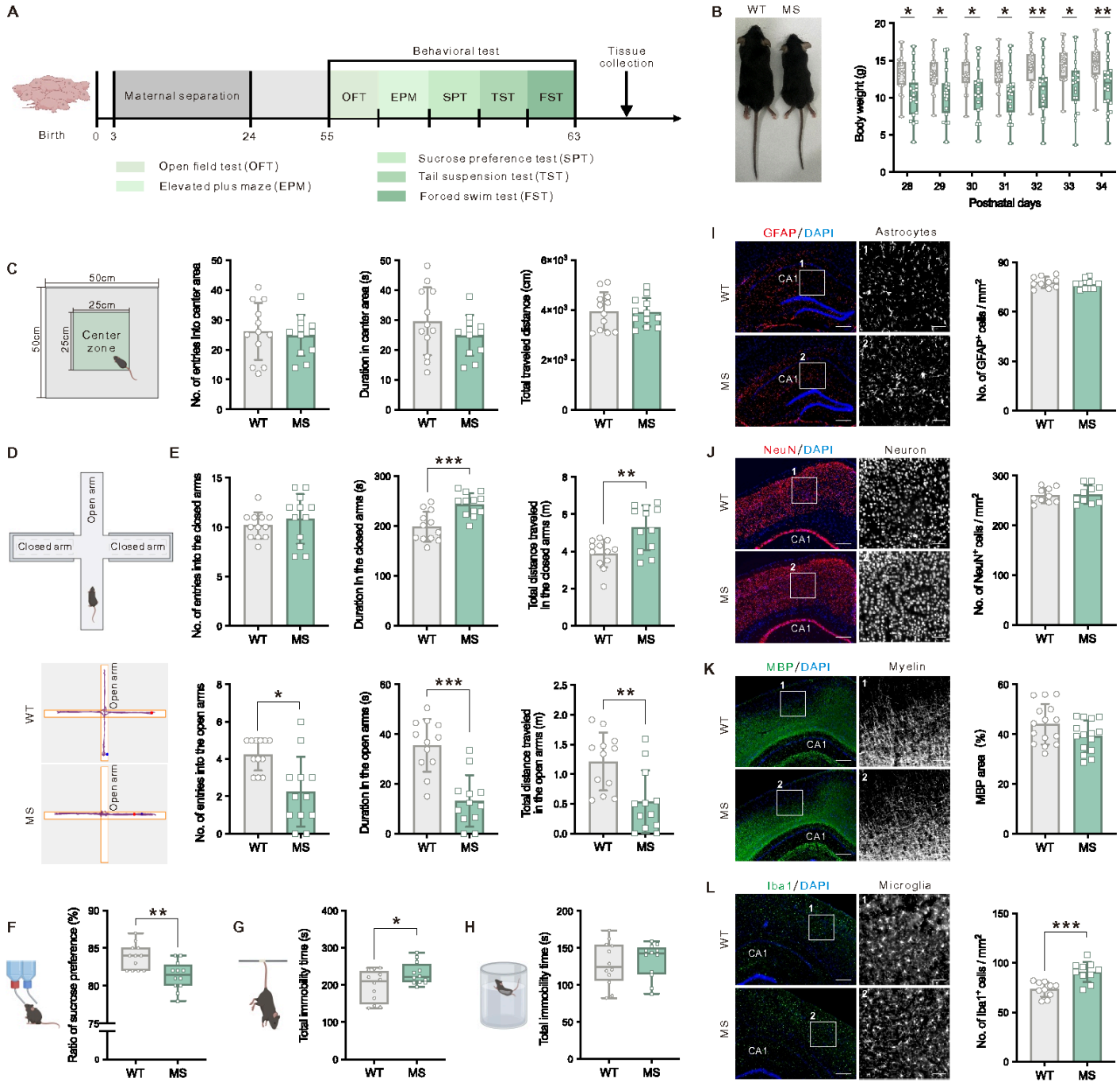


Figure 1

Early-life stress induces anxiety-like behavior accompanied by increased microglial abundance.

(**A**) Schematic diagram illustrating the timeline of neonatal maternal separation and the experimental procedures for behavioral testing. (**B**) Representative photographs of control and MS mice at 1 month of age (left). Box-and-whisker plot presenting body weight distribution in each group (right). *n* = 20 mice per group; two-way ANOVA followed by Sidak's multiple comparisons test; $F_{interaction}(6, 266) = 0.04744$, *P* =

0.9996; $F_{treatment}(6, 266) = 1.972$, $P = 0.0699$; $F_{time}(1, 266) = 65.54$, $P < 0.0001$. (**C**) Schematic diagram of the OFT apparatus (left). Bar graphs showing the number of center entries, duration spent in the center area, and total distance traveled (cm) during the 15-min OFT session (right). *n* = 12 mice per group; unpaired two-tailed Student's *t*-test; the number of center entries: $t(22) = 0.3915$, $P = 0.6992$; duration spent in the center area: $t(22) = 1.240$, $P = 0.2279$; total distance traveled: $t(22) = 0.1730$, $P = 0.8643$. (**D**) Schematic diagram of the EPM apparatus (up) and representative movement trajectories of mice during the 5-min test (down). (**E**) Bar graphs showing the number of entries, time spent, and total distance traveled (m) in the closed arms (up) and open arms (down), respectively. *n* = 12 mice per group; two tailed Welch's correction, the number of closed arms entries, $t(16.75) = 0.8104$; $P = 0.4291$; two tailed Kolmogorov-Smirnov test, the number of open arms entries, D = 0.5833; $P = 0.0337$; unpaired two-tailed Student's *t*-test; duration in the closed arms, $t(22) = 4.083$, $P = 0.0005$; total distance traveled in the closed arms, $t(22) = 3.373$; $P = 0.0027$; duration in the open arms, $t(22) = 5.270$, $P < 0.0001$; total distance traveled in the closed arms, $t(22) = 3.278$, $P = 0.0034$. (**F**) Schematic diagram of the SPT (left). Box-and-whisker plot showing the ratio of sucrose preference (right). *n* = 12 mice per group; unpaired two-tailed Student's *t*-test; $t(22) = 3.425$, $P = 0.0024$. (**G**) Schematic diagram of the TST (left). Box-and-whisker plot showing the total immobility time during 6-min test (right). *n* = 12 mice per group; unpaired two-tailed Student's *t*-test; $t(22) = 2.253$, $P = 0.0346$. (**H**) Schematic diagram of the FST (left). Box-and-whisker plot showing the total immobility time during 4-min test (right). *n* = 12 mice per group; unpaired two-tailed Student's *t*-test; $t(22) = 0.4207$, $P = 0.6781$. (**I-L**) Representative immunofluorescent images showing the density of neurons, astrocytes, myelin, and microglia, visualized by NeuN (**I**), GFAP (**J**), MBP (**K**), and Iba1 (**L**), respectively. Scale bars, 300 μm (left) and 50 μm (right). Bar graph in the right panel shows the number of GFAP-, NeuN-, and Iba1-positive cells per mm^2, and the ratio of MBP-positive area per mm^2 (right). For I-L, *n* = 10-15 region of interests (ROIs) from three biological samples; unpaired two-tailed Student's *t*-test. I, $t(18) = 0.8325$, $P = 0.416$; J, $t(18) = 0.2918$, $P = 0.7738$; K: $t(28) = 1.836$, $P = 0.077$; L: $t(18) = 4.339$, $P = 0.0004$. For box-and-whisker plots, data are presented as minimum to maximum values with the interquartile range and median; for bar graphs, data are presented as mean ± SD; $^*P < 0.05$, $^{**}P < 0.01$, and $^{***}P < 0.001$. The results of the normality and homogeneity of variance tests, statistical methods, and exact P values are listed in Supplementary Table 2.

Figure 2

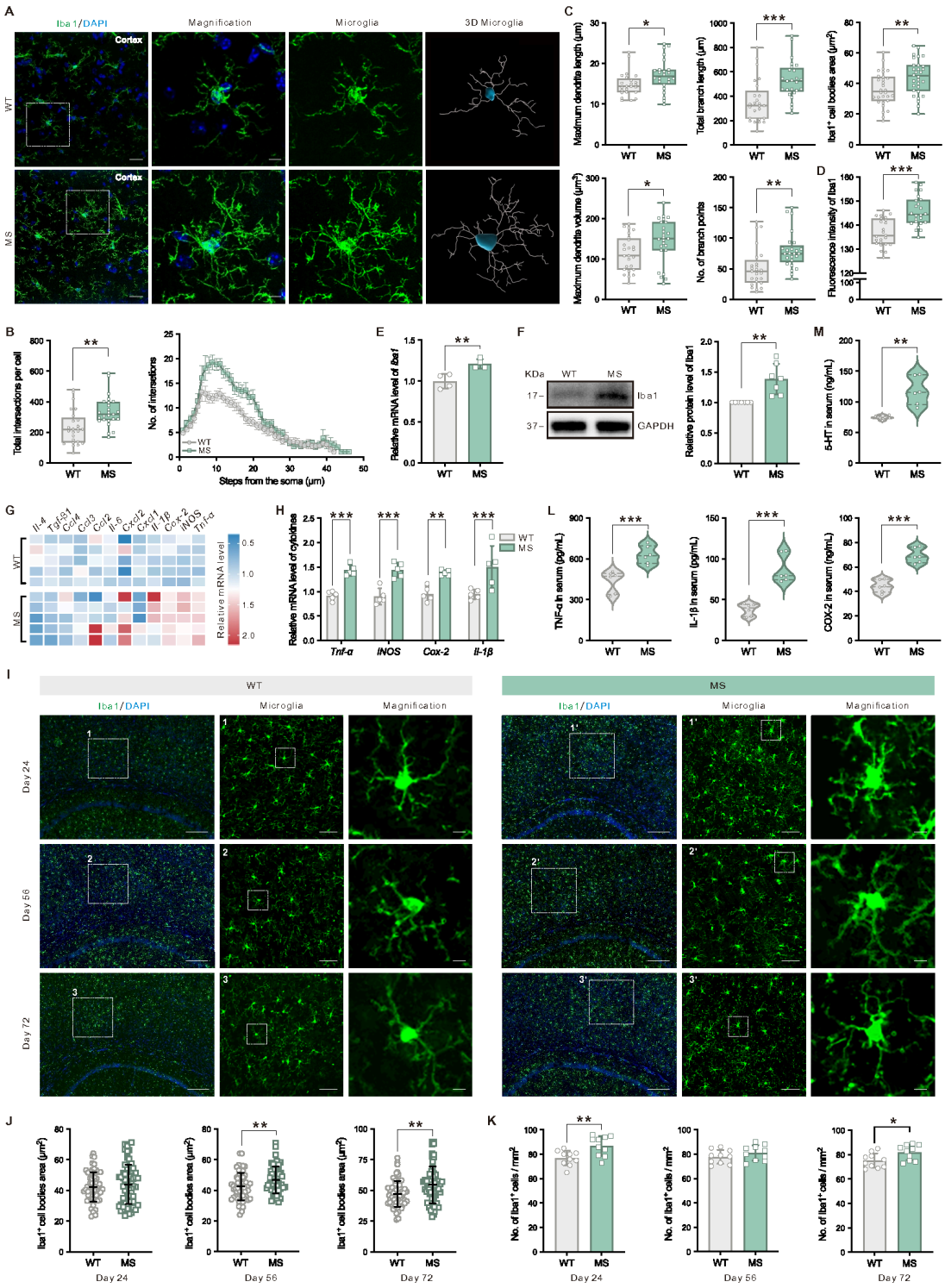


Figure 2

MS-induced microglial activation is associated with widespread neuroinflammatory responses.

(**A**) Representative immunofluorescent images showing microglial morphology and intensity in the cortex. Scale bar: 20 μm. The right panels display higher-magnification views of the selected region from the left image, along with 3D reconstructions of microglial morphology. Scale bar: 5 μm. (**B**-**C**) Box-and-

whisker plots showing quantification of microglial morphology based on Sholl analysis, including the number of intersections (B), as well as dendritic length, volume, branch length, branch number, and cell body size (C). For B, n = 25 ROIs from three biological samples; unpaired two-tailed Student's t-test; $t(48) = 3.417$, $P = 0.0013$; for C, n = 24-30 ROIs from three biological samples; unpaired two-tailed Student's t-test; maximum dendrite length: $t(46) = 2.284$, $P = 0.027$; maximum dendrite volume: $t(48) = 2.226$, $P = 0.0308$; $Iba1^+$ cell bodies volume: $t(58) = 2.747$, $P = 0.008$; two tailed Mann-Whitney U test; total branch length: $U = 133$, $P = 0.0003$; no. of branch points: $U = 136$, $P = 0.0004$. Concentric circles radiate from the soma with radial intervals of 1 μm. (**D**) Box-and-whisker plot showing changes in Iba1 fluorescence intensity. n = 24 ROIs from three biological samples; unpaired two-tailed Student's t-test; $t(46) = 5.032$, $P < 0.0001$. (**E**) Bar showing *Ibal* mRNA level in the mouse cortical region. n= 4 independent quantitative measures from three independent biological samples; unpaired two-tailed Student's t-test; $t(6) = 4.112$; $P = 0.0063$. (**F**) Representative western blots (left) and quantification (right) showing Iba1 protein level in the mouse cortical region. n=7 independent quantitative measures from three independent biological samples; two tailed Welch's correction; $t(6) = 4.047$; $P = 0.0067$. (**G**-**H**) Heatmap (G) and quantification (H) showing mRNA expression level of inflammatory cytokines. n= 5 independent quantitative measures from three independent biological samples; two-way ANOVA followed by Sidak's multiple comparisons test; $F_{interaction}(3, 32) = 0.2011$, $P = 0.8948$; $F_{treatment}(3, 32) = 0.1951$, $P = 0.8990$; $F_{inflammatory}(1, 32) = 71.10$, $P < 0.0001$. (**I**) Representative immunofluorescent images showing microglial morphology in the cortex at postnatal days 24, 56, and 72, respectively. Scale bars, 300 μm (low-magnification images), 50 μm (magnified images), and 5 μm (single-microglia magnification). (**J**) Scatter plot showing the volume of Iba1-positive microglia. n = 60 microglia from three biological samples; for D24, two tailed Welch's correction; $t(109.3) = 0.7770$, $P = 0.4388$; D56, unpaired two-tailed Student's t-test; $t(118) = 2.726$, $P = 0.0074$; D72, two tailed Kolmogorov-Smirnov test; $D = 0.3000$, $P = 0.0090$. (**K**) Bar graph showing the number of Iba1-stained cells in the mouse cortical region. n = 10 ROIs from three mice per group; unpaired two-tailed Student's t-test. For D24, $t(18) = 3.111$, $P = 0.006$; D56, t(18) = 1.233, $P = 0.2334$; D72, $t(18) = 2.493$, $P = 0.0226$. (**L**) Violin plots showing serum concentrations of inflammatory cytokines. n = 6 independent biological samples; two tailed Mann-Whitney U test; for TNF-α, $U = 0$, $P = 0.0022$; IL-1β, $U = 0$, $P = 0.0022$; unpaired two-tailed Student's t-test; COX-2, $t(10) = 7.779$, $P < 0.0001$. (**M**) Violin plots showing serum concentrations of immunomodulator 5-HT. n= 6 independent biological samples; two tailed Welch's correction; $t(5.172) = 4.574$, $P = 0.0055$. For box-and-whisker plots, data are presented as minimum to maximum values with the interquartile range and median; for violin plots show the full data distribution as a density curve, with minimum, maximum, median, and quartile range; wider regions indicate more data points, narrower regions fewer; for bar graphs, data are presented as mean ± SD; *P < 0.05, **P < 0.01, and ***P < 0.001. The results of the normality and homogeneity of variance tests, statistical methods, and exact P values are listed in Supplementary Table 2.

Figure 3

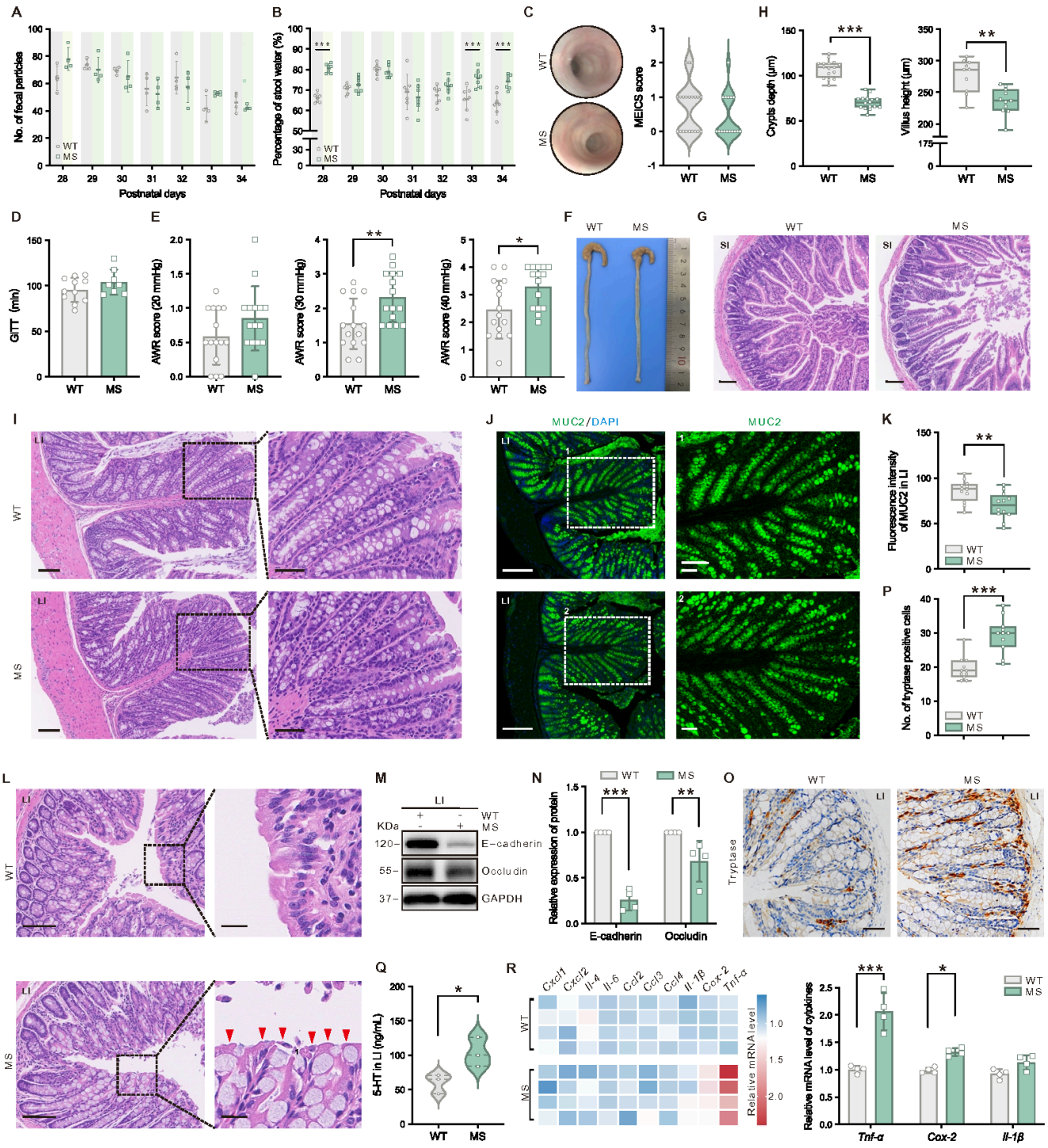


Figure 3

MS-induced chronic neuroinflammation is accompanied by IBS-like gut dysfunction.

(**A**) Scatter plot showing the total number of fecal particles excreted by five mice over a 4-h period. n = 4 groups (five mice per group) for both control and MS groups; two-way ANOVA followed by Sidak's multiple comparisons test; $F_{interaction}(6, 42) = 1.824$, $P = 0.1176$; $F_{treatment}(6, 42) = 13.22$, $P < 0.0001$;

$F_{time}(1, 42) = 0.02346$, $P = 0.8790$. (**B**) Scatter plot showing the percentage of water content of fecal particles. $n = 7$ fecal samples randomly collected from four groups in (A); two-way ANOVA followed by Sidak's multiple comparisons test; $F_{interaction}(6, 84) = 6.923$, $P < 0.0001$; $F_{treatment}(6, 84) = 9.900$, $P < 0.0001$; $F_{time}(1, 84) = 34.04$, $P < 0.0001$. (**C**) Representative endoscopic images of colon (left) and corresponding MEICS scores (right) for the two groups. $n = 16$-21 mice per group; two tailed Mann-Whitney U test; $U = 9$, $P = 0.053$. (**D**) Bar graph showing GITT of two groups. $n = 8$-11 mice per group; unpaired two-tailed Student's t-test; $t(17) = 1.332$, $P = 0.2003$. (**E**) Bar graph showing the AWR scores of mice in response to graded colorectal distention pressures (20, 30, and 40 mmHg). $n = 15$ mice per group; two tailed Mann-Whitney U test; for 20 mmHg, $U = 79$, $P = 0.1550$; 30 mmHg, $U = 47.5$, $P = 0.0053$; 40 mmHg, $U = 55.5$, $P = 0.016$. (**F**) Representative images of colons from control and MS groups. (**G**) Representative H&E-stained microphotographs of the small intestine (SI) showing its architecture and cellular morphology. Scale bars, 100 μm. (**H**) Box-and-whisker plot showing crypt depth and villus height in the SI of mice. $n = 10$-16 ROIs from three biological samples; unpaired two-tailed Student's t-test; for crypts depth, $t(30) = 12.26$, $P < 0.0001$; villus height, $t(19) = 3.867$, $P = 0.001$. (**I**) Representative H&E-stained microphotographs displaying the architecture and cellular morphology of the large intestine (LI). Scale bars, 100 μm (lower-magnification images) and 50 μm (higher-magnification images). (**J**) Representative immunofluorescent images showing MUC2 staining intensity in the LI of mice. Scale bars, 200 μm (lower-magnification images) and 5 μm (higher-magnification images). (**K**) Box-and-whisker plot showing quantified MUC2 fluorescence intensity. $n = 12$ ROIs from three biological samples; unpaired two-tailed Student's t-test; $t(22) = 2.959$, $P = 0.0072$. (**L**) Representative H&E-stained microphotographs showing the architecture and cellular morphology in transverse sections of the LI. The thinned mucus layer in the MS group is highlighted by red arrows in the higher-magnification images. Scale bars, 100 μm (lower-magnification images) and 20 μm (higher-magnification images). (**M**-**N**) Representative western blots (M) and quantification (N) showing the protein level of E-cadherin and Occludin in the mouse LI. $n = 4$ independent biological samples; two-way ANOVA followed by Sidak's multiple comparisons test; $F_{interaction}(1, 12) = 11.29$, $P = 0.0057$; $F_{treatment}(1, 12) = 11.29$, $P = 0.0057$; $F_{protein}(1, 12) = 70.82$, $P < 0.0001$. (**O**) Representative immunohistochemistry images showing tryptase-positive cells in the colon. Scale bar, 50 μm. (**P**) Box-and-whisker plot showing the number of tryptase-positive cells in the colonic mucosal tissue. $n = 11$ ROIs from three biological samples; unpaired two-tailed Student's t-test; $t(20) = 5.280$, $P < 0.0001$. (**Q**) Violin plot showing the concentration of 5-HT in the LI. $n = 3$ independent biological samples; unpaired two-tailed Student's t-test; $t(4) = 2.924$, $P = 0.0431$. (**R**) Heatmap (left) and quantification (right) showing mRNA expression level of inflammatory cytokines in the intestine. $n = 4$ independent biological samples; two-way ANOVA followed by Sidak's multiple comparisons test. $F_{interaction}(2, 18) = 16.14$, $P < 0.0001$; $F_{treatment}(2, 18) = 21.54$, $P < 0.0001$; $F_{inflammatory}(1, 18) = 66.92$, $P < 0.0001$. For box-and-whisker plots, data are presented as minimum to maximum values with the interquartile range and median; for violin plots show the full data distribution as a density curve, with minimum, maximum, median, and quartile range; wider regions indicate more data points, narrower regions fewer; for bar graphs, data are presented as mean ± SD; *$P < 0.05$, **$P < 0.01$, and ***$P < 0.001$.

The results of the normality and homogeneity of variance tests, statistical methods, and exact P values are listed in Supplementary Table 2.

Figure 4

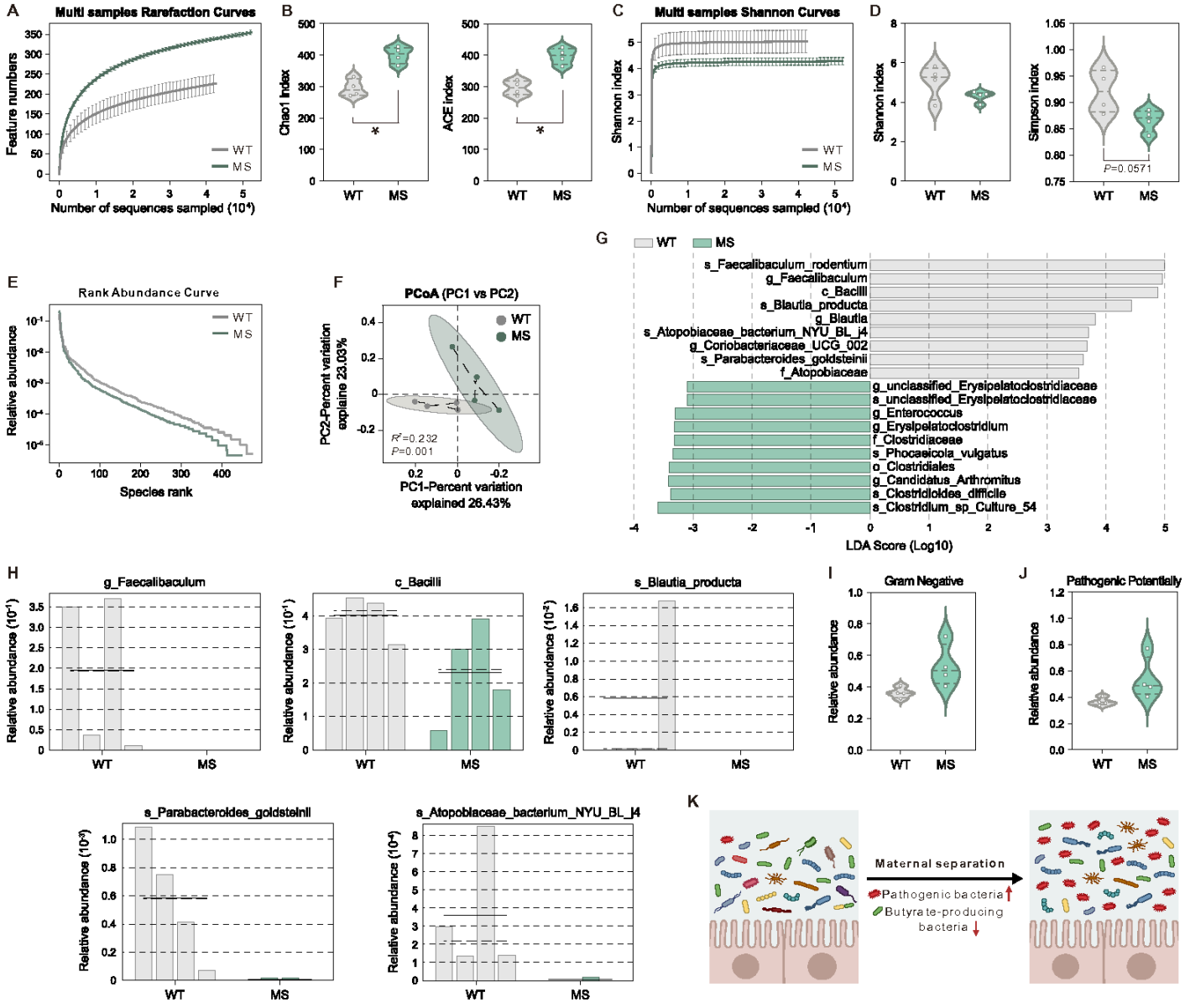


Figure 4

MS-induced gut dysfunction is associated with dysbiosis, promoting a pro-inflammatory state.

(**A**) Rarefaction curves showing bacterial richness of fecal samples based on 16S rRNA gene sequencing. (**B**) Violin plots comparing microbial richness (Chao1 and ACE indices) between control and MS mice in alpha diversity analysis. *n* = 4 independent biological fecal samples; two tailed Mann-Whitney *U* test; for Chao1, *U* = 0; *P* = 0.0286; ACE, *U*= 0, *P* = 0.0286. (**C**) Shannon diversity curves illustrating microbial diversity. (**D**) Violin plots showing microbial community diversity and evenness (Simpson and Shannon indices) between control and MS mice. *n* = 4 independent biological fecal samples; two tailed

Mann-Whitney *U* test; for Simpson, *U*=1, *P* = 0.0571; Shannon, *U* = 4, *P* = 0.3429. (**E)** Rank-abundance (Whittaker) plots showing a marked increase in microbial richness but a reduced evenness in MS mice. (**F**) PCA scatter plot showing clustering of fecal samples between control and MS mice. (**G**) Linear discriminant analysis (LDA) score based on the LEfSe analysis showing gut microbiome bacterial genera in the control group, revealing decreased genera in the MS fecal sample. (**H**) Bar graph showing the relative abundance of bacteria in individual samples. (**I**) Box plot showing the relative abundance of Gram-positive bacteria in colonic mucosa. *n =* 4 independent biological fecal samples; two tailed Kolmogorov-Smirnov test; *D* = 0.7500, *P* = 0.2286. (**J**) Box plot showing the relative abundance of pathogenic bacteria in the colonic mucosa. *n =* 4 independent biological fecal samples; two tailed Kolmogorov-Smirnov test; *D* = 0.7500, *P* = 0.2286. (**K**) Schematic diagram summarizing microbiome alterations induced by maternal separation. For violin plots show the full data distribution as a density curve, with minimum, maximum, median, and quartile range; wider regions indicate more data points, narrower regions fewer; for bar graphs, data are presented as mean ± SD; **P* < 0.05 and ***P* < 0.01. The results of the normality and homogeneity of variance tests, statistical methods, and exact P values are listed in Supplementary Table 2.

Figure 5

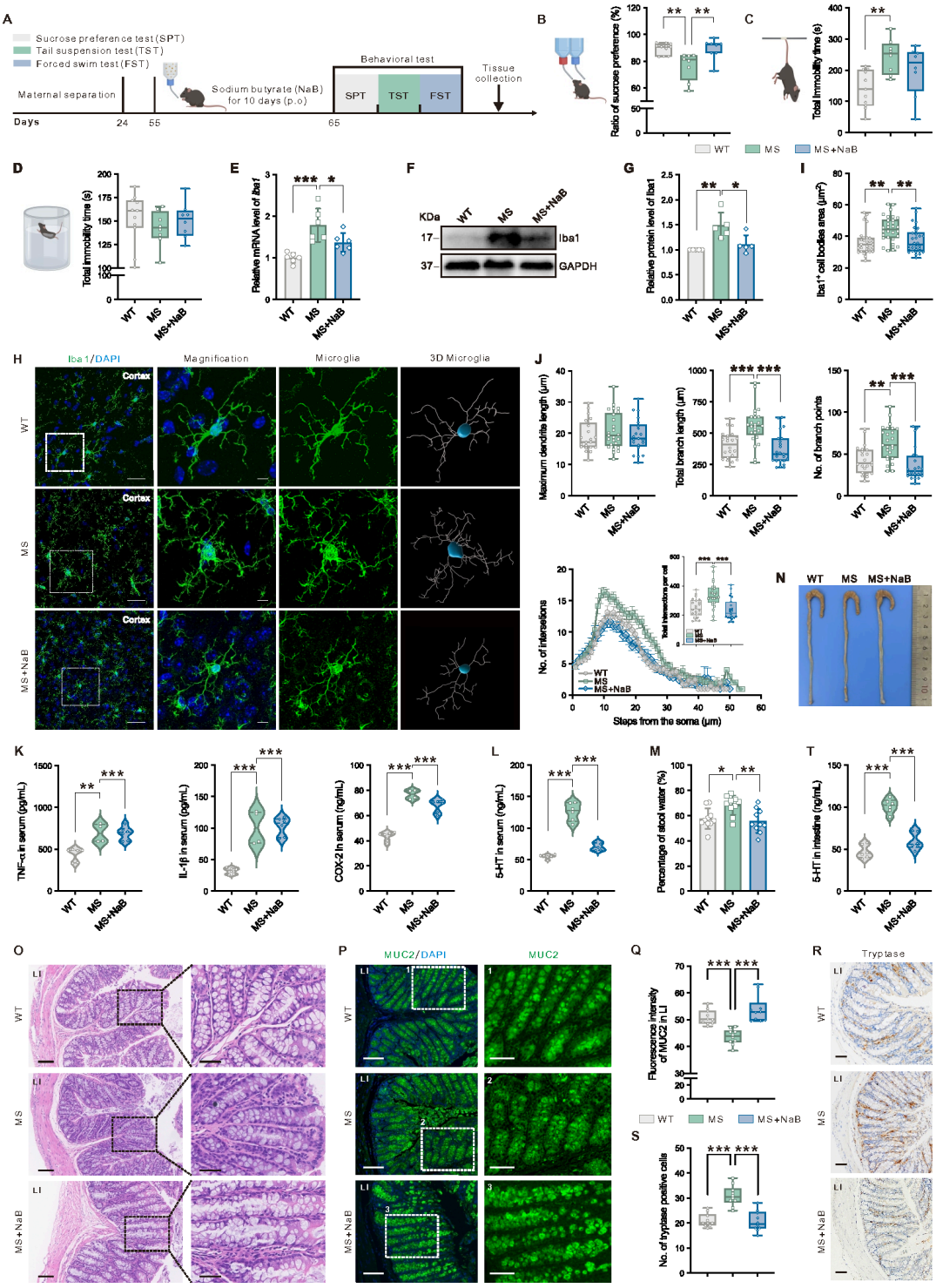


Figure 5

Butyrate treatment ameliorates inflammation-driven brain–gut dysfunction and behavioral abnormalities.

(**A**) Schematic diagram illustrating the timeline of sodium butyrate (NaB) treatment following neonatal maternal separation and the schedule of behavioral tests. After maternal separation, mice in the NaB treatment group (abbreviated as MS+NaB) received oral administration of 200 mM NaB for 10

consecutive days before behavioral testing. (**B**) Schematic diagram of SPT (left) and box-and-whisker plot showing the ratio of sucrose preference (right). *n* = 8-11 mice per group; Kruskal-Wallis followed by Dunn's multiple comparisons test; $F_{treatment}(2, 24) = 8.611$, $P = 0.0015$. (**C**) Schematic diagram of the TST (left) and box-and-whisker plot showing the total immobility time during 6-min test (right). *n* = 8-11 mice per group; Ordinary one-way ANOVA followed by Tukey's multiple comparisons test; $F_{treatment}(2, 24) = 5.947$, $P = 0.0080$. (**D**) Schematic diagram of the FST (left) and box-and-whisker plot showing the total immobility time during the 4-min test (right). *n* = 8-11 mice per group; Ordinary one-way ANOVA followed by Tukey's multiple comparisons test; $F_{treatment}(2, 24) = 0.5292$, $P = 0.5958$. (**E**) Bar graph showing changes in *Ibal* mRNA levels in the mouse cortical region. *n* = 6 independent biological samples; Ordinary one-way ANOVA followed by Tukey's multiple comparisons test; $F_{treatment}(2, 15) = 12.31$, $P = 0.0007$. (**F-G**) Representative western blots (F) and quantification (G) showing the protein level of Ibal in the mouse cortical region. *n* = 5 independent biological samples; Ordinary one-way ANOVA followed by Tukey's multiple comparisons test; $F_{treatment}(2, 12) = 9.576$, $P = 0.0033$. (**H**) Representative immunofluorescent images showing microglial morphology and intensity in the cortex. Scale bars, 20 μm (low-magnification images) and 5 μm (single-microglia magnification). (**I-J**) Box-and-whisker plots showing quantification of microglial morphology based on Sholl analysis, including cell body size (I), as well as the number of intersections, dendritic length, volume, branch length, and branch number (J). Concentric circles radiate from the soma with radial intervals of 1 μm. For I, *n* = 30 microglia from three biological samples; Kruskal-Wallis followed by Dunn's multiple comparisons test; $F_{treatment}(2, 87) = 8.342$, $P = 0.0005$; J, *n* = 22-25 microglia from three biological samples; Kruskal-Wallis followed by Dunn's multiple comparisons test; maximum dendrite length, $F_{treatment}(2, 64) = 0.6845$, $P = 0.5080$; total branch length: $F_{treatment}(2, 67) = 15.49$, $P < 0.0001$; number of branch points, $F_{treatment}(2, 67) = 12.32$, $P < 0.0001$. (**K**) Violin plots showing serum concentrations of inflammatory cytokines. *n* = 4-6 independent biological samples; Kruskal-Wallis followed by Dunn's multiple comparisons test; for TNF-α, $F_{treatment}(2, 13) = 15.16$, $P = 0.0004$; Ordinary one-way ANOVA followed by Tukey's multiple comparisons test; Welch's ANOVA followed by Dunnett's T3 multiple comparisons test; IL-1β: $F_{treatment}(2, 13) = 34.32$, $P < 0.0001$; COX-2, $F_{treatment}(2, 13) = 84.93$, $P < 0.0001$. (**L**) Violin plots showing serum concentrations of immunomodulator 5-HT. *n* = 5-6 independent biological samples; Welch's ANOVA followed by Dunnett's T3 multiple comparisons test; $F_{treatment}(2, 14) = 94.73$, $P < 0.0001$. (**M**) Bar graph showing the percentage of water content of fecal particles. *n* = 10 fecal samples randomly collected from each group; Ordinary one-way ANOVA followed by Tukey's multiple comparisons test; $F_{treatment}(2, 27) = 6.577$, $P = 0.0047$. (**N**) Representative images of colons from control, MS, and MS+NaB groups. (**O**) Representative H&E-stained microphotographs displaying the architecture and cellular morphology of the LI. Scale bars, 100 μm (lower-magnification images) and 50 μm (higher-magnification images). (**P**) Representative immunofluorescent images showing MUC2 staining intensity in the LI of mice. Scale bars, 100 μm (lower-magnification images) and 50 μm (higher-magnification images). (**Q**) Box-and-whisker plot showing quantified MUC2 fluorescence intensity. *n* = 10 ROIs from three biological samples; Ordinary one-way ANOVA followed by Tukey's multiple comparisons test; $F_{treatment}(2, 27) = 20.14$, $P < 0.0001$. (**R**) Representative immunohistochemistry images showing tryptase-positive cells in the colon. Scale bar, 50

μm. (**S**) Box-and-whisker plot showing the number of tryptase-positive cells in the colonic mucosal tissue. *n* = 10 ROIs from three biological samples; ordinary one-way ANOVA. Ordinary one-way ANOVA followed by Tukey's multiple comparisons test; $F_{treatment}(2, 27) = 25.14$, $P < 0.0001$. (**T**) Violin plot showing intestinal concentration of 5-HT. *n* = 6 independent biological samples; ordinary one-way ANOVA. Ordinary one-way ANOVA followed by Tukey's multiple comparisons test; $F_{treatment}(2, 15) = 61.99$, $P < 0.0001$. For box-and-whisker plots, data are presented as minimum to maximum values with the interquartile range and median; for violin plots show the full data distribution as a density curve, with minimum, maximum, median, and quartile range; wider regions indicate more data points, narrower regions fewer; for bar graphs, data are presented as mean ± SD; *$P < 0.05$, **$P < 0.01$, and ***$P < 0.001$. The results of the normality and homogeneity of variance tests, statistical methods, and exact P values are listed in Supplementary Table 2.

Supplementary Files

This is a list of supplementary files associated with this preprint. Click to download.

- SupplementaryTable1.xlsx
- SupplementaryTable2.xlsx
- Supplementaryinformation.pdf
- Graphicabstract.docx